

**Master's thesis**

# **Optimization of the electrical Rydberg signal for a nitric oxide trace-gas sensor**

**Author:** Alexander Trachtmann

**Examiner:** Prof. Dr. Tilman Pfau

**Co-Examiner:** Prof. Dr. Jörg Wrachtrup

**Supervisor:** Fabian Munkes

Submitted to the  
5th Institute of Physics  
University of Stuttgart  
Pfaffenwaldring 57  
70569 Stuttgart

December 22, 2023



# Zusammenfassung

## Einführung

Diese Masterarbeit entstand im Rahmen des Projekts "QNOSE" (*quantum nitric oxide sensing experiment*) am 5. Physikalischen Institut an der Universität Stuttgart. Das übergreifende Ziel ist die Entwicklung eines Spurengassensors für Stickstoffmonoxid (NO).

NO spielt eine wichtige Rolle in zahlreichen physiologischen Prozessen wie Gefäßerweiterung, Neurotransmission, Apoptose, Tumorwachstum und Entzündungen [1]. Die Ausatemluft des Menschen enthält eine NO-Konzentration im Milliardenstel Bereich (*parts per billion*) [2]. Im Falle einer entzündlichen Erkrankung wie Asthma ist die NO-Konzentration in der Ausatemluft erhöht [3]. Das begründet eine mögliche medizinische Anwendung des NO-Spurengassensors. Aufgrund der elektronischen Struktur von NO, die die Anregung eines einzelnen Elektrons zu einem hoch angeregten Zustand, dem so genannten Rydberg-Zustand ermöglicht, eröffnen sich interessante physikalische Aspekte für Untersuchungen. In [4] wird zum Beispiel die Bildung eines Rydberg-Bimoleküls von NO theoretisch gezeigt.

Das Funktionsprinzip unseres Sensors basiert auf einer Drei-Photonen-Anregung mit Dauerstrich-Lasersystemen. So wird das einzige freie Außenelektron von NO zu einem Rydberg-Zustand angeregt. Anschließende Kollisionen mit Hintergrundteilchen führen zur Ionisation. Die Ladungen werden durch Anlegen eines elektrischen Feldes getrennt. Eine elektrische Schaltung mit einem Transimpedanzverstärker wandelt den Ionisationsstrom in eine messbare Spannung um. Nach diesem Prinzip kann NO elektronisch detektiert werden. Ein Vorteil der elektrischen Auslesung, nämlich eine bessere Signalqualität im Vergleich zu rein optischen Techniken, wurde in [5] demonstriert. Ein Konzeptnachweis für einen optogalvanischen Sensor wurde in [6] gezeigt. Das Sensorprinzip erlaubt den Nachweis von NO bei einer Konzentration von weniger als 10 Teilen pro Million (*parts per million*).

Das Sensorprinzip hat viele Vorteile. Das Drei-Photonen-Anregungsschema ermöglicht eine hohe Selektivität bei der NO-Detektion. Die Verwendung von Dauerstrich-Lasern führt zu einer schmalen Linienbreite, die ebenfalls zu einer hohen Selektivität und Empfindlichkeit des Spurengassensors beiträgt. Eine schmale Linienbreite ist für verschiedene Untersuchungen notwendig, zum Beispiel für Messungen in Abhängigkeit vom elektrischen Feld, die auch im Laufe dieser Arbeit gemacht wurden. Hier ist eine hohe Auflösung vor allem bei kleinen elektrischen Feldern wichtig. Ein weiterer Vorteil

---

des verwendeten Sensors ist, dass nur ein kleines Gasvolumen für die Detektion benötigt wird. Das Gasvolumen, das derzeit für den Nachweis von NO nötig ist, liegt in einem Bereich von unter einem Milliliter. Außerdem erfolgt der Nachweis von NO fast instantan, im Bereich von Millisekunden. Die aktuelle Detektionseffizienz liegt im Bereich von  $10^{-6}$ .

Die vorliegende Masterarbeit beschäftigt sich mit der experimentellen Optimierung des bereits bestehenden Aufbaus für den optogalvanischen Spurengassensensor von NO und stellt die daraus gewonnenen experimentellen Ergebnisse vor. Der Schwerpunkt der Arbeit lag dabei hauptsächlich auf dem experimentellen Teil.

## Ergebnisse

Im ersten Teil wurden die Kollisionsverbreiterung und Verschiebung von Rydberglinien in NO untersucht. Im Hinblick auf eine Sensoranwendung ist ein Betrieb im Mikrobar-Bereich erstrebenswert, um Verbreiterungseffekte aufgrund von Kollisionen zu minimieren. Elastische Kollisionen sind dominanter, wenn NO mit anderen NO-Molekülen wechselwirkt, im Vergleich zu einer Wechselwirkung von NO mit Stickstoff ( $N_2$ ). Im ersten Fall wurde eine Rotverschiebung der Rydberglinie beobachtet, wenn die Dichte von NO erhöht wird. Im Fall der Wechselwirkung von NO mit zunehmender Dichte von  $N_2$  war nur eine leichte Blauverschiebung in dem untersuchten Dichtebereich sichtbar. Der Nobelpreisträger Enrico Fermi hat schon im Jahr 1934 gezeigt, dass die lineare Dichteabhängigkeit der Verschiebung der spektroskopischen Linie auf elastische Stöße zwischen dem Rydberg-Elektron und einem Störgas zurückzuführen ist [7]. Die aus unseren Messungen extrahierten Verschiebungsraten mit reinem NO liegen in der gleichen Größenordnung, sind jedoch um ein Vielfaches kleiner im Vergleich zu Untersuchungen mit durch Edelgasatome gestörten Alkalielementen [8, 9]. Andererseits sind unsere Verbreiterungsraten der Rydberglinien höher. Die Unterschiede lassen sich auf die Komplexität des Molekülspektrums, bedingt durch zusätzliche Freiheitsgrade der Rotation und Vibration zurückführen, die bei einem Atom nicht vorhanden sind.

Im zweiten Teil wurde der Stark-Effekt von mehreren Rydberg-Zuständen von NO untersucht. Optimierungen bezüglich der experimentellen Parameter wurden durchgeführt. Dies ermöglichte die Messung einer hochaufgelösten sogenannten Stark-Map des Rydberg-Zustandes mit der Hauptquantenzahl  $n = 22$  aus der Rotationsserie  $N^+ = 0$ . Unter Berücksichtigung des nichtlinearen elektrischen Feldes in der Messzelle war es möglich, eine theoretische Simulation der Stark-Map an die experimentellen Daten anzupassen. Die Simulation wurde von Prof. Stephen Hogan und Dr. Matthew Rayment von der University College London (UCL) durchgeführt. Schließlich konnte der Quantendefekt des g-Zustandes extrahiert werden. Die Genauigkeit ist höher als die in der Literatur bekannten Werte ([10, 11]). Das Ergebnis für den Quantendefekt ist jedoch noch nicht endgültig.

---

In Zukunft werden weitere Verbesserungen der Eigenschaften des Spurengassensors gemacht. Optimierungen bezüglich des Designs und der elektrischen Schaltung der Messzelle können die Sensitivität des Sensors weiter erhöhen. Zur Verbesserung der Empfindlichkeit können auch andere Rotationszweige für die Anregung in Betracht gezogen werden, da andere Anregungspfade möglicherweise zu höheren Rydberg-Signalen führen. Weitere Verbesserungen der Empfindlichkeit des Sensors könnten den Nachweis des NO-Bimoleküls ermöglichen, welches in [4] theoretisch prognostiziert wurde. Künftige Untersuchungen werden auf den Ergebnissen dieser Arbeit aufbauen, da sie neue Informationen über gute experimentelle Parameter liefert.



# Contents

<b>1</b>	<b>Introduction</b>	<b>1</b>
<b>2</b>	<b>Theoretical background of nitric oxide</b>	<b>3</b>
2.1	Semiclassical description . . . . .	3
2.1.1	Rotational spectrum . . . . .	4
2.1.2	Vibrational spectrum . . . . .	6
2.1.3	Rovibrational spectrum . . . . .	7
2.2	Couplings of angular momenta . . . . .	8
2.2.1	Hund's case (a) . . . . .	8
2.2.2	Hund's case (b) . . . . .	8
2.2.3	Hund's case (d) . . . . .	9
2.3	Excitation of NO . . . . .	10
2.3.1	Labeling of a molecular state . . . . .	11
2.3.2	Rydberg states . . . . .	12
2.3.3	Labeling and excitation scheme of NO . . . . .	13
2.4	Spectroscopic line broadening and shifts . . . . .	17
2.4.1	Line shapes . . . . .	17
2.4.2	Broadening mechanisms . . . . .	18
2.4.3	Collisional shift and broadening . . . . .	19
2.5	Stark effect . . . . .	23
<b>3</b>	<b>Experimental setup and characteristics</b>	<b>27</b>
3.1	Basic working principle . . . . .	27
3.2	Laser setup . . . . .	30
3.2.1	UV laser system . . . . .	30
3.2.2	Green laser system . . . . .	30
3.2.3	Infrared laser system . . . . .	31
3.2.4	Power stabilization and regulation . . . . .	31
3.2.5	Frequency stabilization . . . . .	32
3.3	Gas mixing setup . . . . .	34
3.3.1	Mass flow controllers . . . . .	34
3.3.2	Pump system . . . . .	35
3.3.3	Experimental details . . . . .	35
3.4	Experimental measurement cell . . . . .	36
3.4.1	Electric field . . . . .	36
3.4.2	Electronic limits due to the TIA . . . . .	37

3.5	Experimental procedure . . . . .	39
3.5.1	Calculation of the transition wavelengths . . . . .	39
3.5.2	Setting up the measurement . . . . .	40
3.5.3	Data evaluation . . . . .	42
<b>4</b>	<b>Experimental results</b>	<b>43</b>
4.1	Collisional shift and broadening . . . . .	43
4.1.1	Pressure dependent measurement procedure . . . . .	43
4.1.2	Evaluation . . . . .	45
4.1.3	Results . . . . .	48
4.1.4	Conclusion . . . . .	51
4.2	Stark effect . . . . .	53
4.2.1	Electric field dependent measurement . . . . .	53
4.2.2	Evaluation . . . . .	54
4.2.3	Results . . . . .	55
4.2.4	Conclusion . . . . .	62
<b>5</b>	<b>Summary and outlook</b>	<b>63</b>

# 1 Introduction

This master's thesis has been created in the scope of the QNOSE (*quantum nitric oxide sensing experiment*) project at the 5th Institute of Physics at the University of Stuttgart. As the project's name suggests, the ultimate goal is the development of a nitric oxide (NO) trace-gas sensor.

NO has an important role in signaling pathways involved in several physiological processes like vasodilation, neurotransmission, apoptosis, tumor growth, and inflammation [1]. The exhaled air of humans contains a concentration of NO in the parts-per-billion regime [2]. In the case of an inflammatory disease like asthma, the concentration of NO in the exhaled air is increased [3]. Thus, an NO trace-gas sensor has a medical application. Furthermore, due to the electronical structure of NO allowing the excitation of a single free electron to a highly excited state, a so-called Rydberg state, opens up interesting physical aspects to study. For example, in [4] the formation of an ultralong-range Rydberg bimolecule of NO has been theoretically shown.

The working principle of our sensor is based on a three-photon excitation scheme involving continuous-wave laser systems. Thus, the single free outer electron of NO is excited to a Rydberg state and is likely to be ionized due to collisions with background particles. The charges are separated by applying an electric field. An electrical circuit including a transimpedance amplifier converts the ionization current to a measurable voltage. Following this principle, NO can be electronically detected. An advantage of the electrical readout, namely a better signal quality compared to purely optical techniques, has been demonstrated in [5]. A proof-of-concept for the optogalvanic sensing method of NO has been shown in [6]. This sensing principle allows to detect NO concentrations less than 10 parts-per-million.

The sensing principle offers many advantages. The three-photon excitation scheme provides a high selectivity of NO. Using continuous-wave laser systems yields a sharp linewidth which contributes to a high selectivity and sensitivity of the trace-gas sensor. A sharp linewidth is also important for several kinds of investigations like electric field-dependent measurements presented later on, where a high resolution at small electric fields is important. Another advantage of the sensor in use is that only a small gas volume is required for the detection. The gas volume that is currently needed to detect NO is in a range below a milliliter. Further, the detection of NO happens quite instantaneous, in the range of milliseconds. Currently, the detection efficiency is in the range of  $10^{-6}$ .

The work done in the scope of this thesis deals with the experimental optimization of the already existent setup and presents subsequently gained experimental results. An

outline of the structure of this thesis is given in the following. The focus of this work was mainly on the experimental part. However, a theoretical introduction necessary for understanding this work is given in chapter 2. Here, the rovibrational spectrum, the relevant angular momenta, as well as the excitation scheme of NO are explained. Moreover, spectroscopic line broadening and shifts along with the Stark effect are introduced. These mechanisms, which are in the first case pressure dependent and in the latter one electric field dependent, are important in regard to the results presented later on. Chapter 3 introduces the experimental setup, which includes three main elements, namely the laser setup, the gas mixing unit, and the measurement cell. Details on the experimental procedure are given as well. The final results presented in chapter 4 may be broken down into two main topics. First, measurement results of collisional shifts and broadening are shown. Here, Rydberg states of NO under perturbation of NO itself or nitrogen ( $N_2$ ) are investigated. The main compound of the exhaled breath volume is  $N_2$  [12]. The results gained are important in terms of a sensor application. They can also be classified physically. Elastic scattering processes involved have been studied theoretically back in 1934 by the Nobel laureate Enrico Fermi [7]. The second part of the results presented deals with the Stark effect. The experimental data gained after the optimization gives rise to in-depth theoretical investigations namely the g-state quantum defect. The latter is done by our cooperation partners Prof. Stephen Hogan and Dr. Matthew Rayment at the University College London. The results of this thesis are summarized in chapter 5.

## 2 Theoretical background of nitric oxide

This chapter summarizes the theoretical background necessary for this work. As introduced, the molecule of interest is nitric oxide (NO). While an individual atom consists of a single nucleus surrounded by electrons, a molecule is an assembly of many nuclei. This gives rise to additional degrees of freedom, apart from translational motion, which results in complex molecular spectra. A molecule with  $n$  atoms has  $3n$  degrees of freedom. There are 3 translational and rotational degrees of freedom. The entire molecule can move freely and rotate around the three spatial axes. Thus, there are  $3n - 6$  vibrational degrees of freedom left. This only holds for  $n \geq 3$ . NO is a diatomic heteronuclear molecule. Here, 2 rotational and one vibrational degrees of freedom are available. The rotation around the molecular axis is suppressed. An insight into diatomic molecular theory is given in the following. This chapter is mainly based on [13, 14].

### 2.1 Semiclassical description

Since the mass of a nucleus is several orders of magnitude larger than the electron's mass, the electron's wavefunction can be approximated as being independent of nuclear momenta, allowing a separate treatment. Couplings of the motions of the electrons and nuclei are neglected in the first place. This is referred to as the Born-Oppenheimer approximation [15], which is used in the scope of the derivation of the nuclear Schrödinger equation. The total wavefunction  $\psi$  is approximated by the product of the eigenfunctions of the electronic and nuclear Hamiltonians

$$\psi = \phi_{\text{el}} \cdot \phi_{\text{N}}. \quad (2.1)$$

Then, the nuclear Schrödinger equation of a diatomic molecule reads [14]

$$\left( -\frac{\hbar^2}{2\mu} \nabla_{\mathbf{R}}^2 + E_{\text{el}}(\mathbf{R}) + V(\mathbf{R}) \right) \phi_{\text{N}}(\mathbf{R}) = E_{\text{N}} \phi_{\text{N}}(\mathbf{R}). \quad (2.2)$$

The first term in equation (2.2) describes the kinetic part of the nuclear Hamiltonian. The reduced nuclear mass is  $\mu = (M_1 \cdot M_2) \cdot (M_1 + M_2)^{-1}$ , where  $M_i$  are the individual nuclei's masses.  $\hbar$  is the reduced Planck constant. The second term  $E_{\text{el}}(\mathbf{R})$  is the energy of the electronic state. The internuclear vector is  $\mathbf{R}$ . The absolute value of this vector

is the internuclear distance  $R$ .  $V(\mathbf{R})$  is the nuclear-nuclear potential energy. The wavefunction  $\phi_N(\mathbf{R})$  is the nuclear part of the total wavefunction and  $E_N$  is the corresponding eigenenergy.

The total energy  $E$  of a molecular state is the sum of the electronic and nuclear energy and is given by

$$E = E_{\text{el}} + E_N. \quad (2.3)$$

The nuclear energy  $E_N$  has a vibrational ( $E_{\text{vib}}$ ) and rotational contribution ( $E_{\text{rot}}$ ). Typically, the molecular energy is given in units of wavenumbers ( $\text{cm}^{-1}$ ). Thus, the total energy can be expressed by

$$\frac{E}{hc} = \frac{E_{\text{el}}}{hc} + \frac{E_{\text{vib}}}{hc} + \frac{E_{\text{rot}}}{hc} \quad (2.4)$$

$$\equiv T_{\text{el}} + G + F. \quad (2.5)$$

$T_{\text{el}}$ ,  $G$ , and  $F$  describe the respective energy terms. Here,  $h$  is the Planck constant and  $c$  is the speed of light.

The next subsections give a short derivation of the nuclear energy terms, based on a classical approach.

### 2.1.1 Rotational spectrum

Starting from classical physics, the rotational energy can be calculated by considering the diatomic molecule as a rigid rotator. This is referred to as the dumbbell model [13]. A sketch of the rigid rotator is shown in figure 2.1.1. The molecule is described by two point-like masses which are connected via a rigid rod. The rotational energy in this case is given by

$$E_{\text{rot}}^{(1)} = \frac{1}{2} \Theta \omega^2. \quad (2.6)$$

The rotational angular frequency in reference to the center of mass (COM) is given by  $\omega$ . The moment of inertia regarding the COM and perpendicular to the rigid rod between the two masses is  $\Theta = \mu R_e^2$ . The internuclear distance  $R_e$  is fixed, and the reduced mass of both nuclei is  $\mu$ .

Classically, the magnitude of the angular momentum is given by  $L = \Theta \cdot \omega$ . The eigenvalues of the quantum mechanical angular momentum operator  $\mathbf{L}$  are given by  $L = \hbar \cdot \sqrt{N^+(N^+ + 1)}$ , with  $N^+ = 0, 1, 2, \dots$  being the rotational quantum number. The  $+$  sign is introduced to stress the fact that we are dealing with the positive ionic molecular cores which will be important in regard to Rydberg states described later on. Connecting the classical and quantum mechanical expressions leads to the quantized rotational energy in the first approximation

$$E_{\text{rot}}^{(1)}(N^+) = \frac{\hbar^2}{2\Theta} N^+(N^+ + 1). \quad (2.7)$$

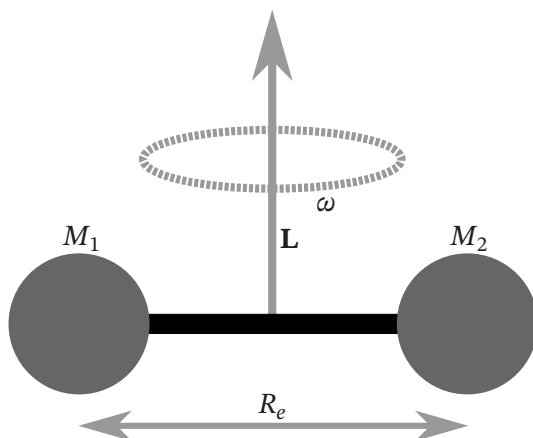


**Figure 2.1.1:** The rigid rotator is shown. The nuclei are connected by a rigid rod with a fixed distance  $R_e$ . For simplicity, the masses of the nuclei are considered to be the same ( $M_1 = M_2$ ), thus the COM is in the middle of the internuclear axis. The rotation around the angular momentum vector, classically denoted by  $\mathbf{L}$  with angular frequency  $\omega$  is depicted as well. If  $M_1 > M_2$  the COM shifts in the direction of  $M_1$ .

The superscript (1) indicates the approximation in first order. Conversion to energy in units of wavenumbers and introducing the rotational constant  $B$  leads to

$$F^{(1)}(N^+) = BN^+(N^+ + 1), \quad B = \frac{\hbar}{4\pi c\Theta}. \quad (2.8)$$

However, a more accurate description is given by considering a non-rigid rotator. A figure is shown in 2.1.2. Due to the rotation of the molecule, the centrifugal force leads to a change in the internuclear distance, if the masses are considered to be connected through an elastic axis. This is modeled by introducing a massless spring with spring constant  $k$  in the scope of the model of a non-rigid rotator. There is an equilibrium between the centrifugal and spring force

$$F_C = F_S, \quad (2.9)$$

$$\mu R\omega^2 = k(R - R_e). \quad (2.10)$$

The actual internuclear distance is  $R$ .  $(R - R_e)$  is the elongation with respect to the equilibrium position at rest. Taylor expansion up to the second order under the assumption of small elongations and by introducing the quantization of the rotation leads to the rotational energy which includes the so-called centrifugal distortion constant  $D$ :

$$F(N^+) = BN^+(N^+ + 1) - D(N^+)^2(N^+ + 1)^2, \quad D = \frac{\hbar^3}{4\pi k\Theta^2 R_e^2 c} \quad (2.11)$$

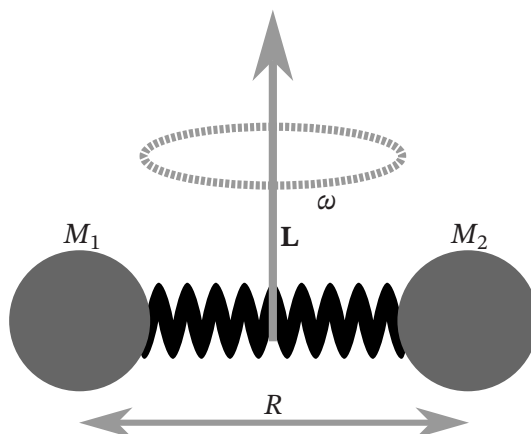


**Figure 2.1.2:** The non-rigid rotator is shown. The nuclei are connected by an elastic spring with distance  $R$ .

### 2.1.2 Vibrational spectrum

Now, the vibrational structure of the diatomic molecule is covered. Based on the elastic spring force between the nuclei as introduced in the previous section 2.1.1, the vibrational energy is classically described by

$$E_{\text{vib}}^{(1)} = \frac{1}{2}k(R - R_e)^2. \quad (2.12)$$

The corresponding energy eigenvalues of the quantized harmonic oscillator are

$$E_{\text{vib}}^{(1)}(v) = \hbar\omega \left( v + \frac{1}{2} \right). \quad (2.13)$$

The vibrational quantum number is  $v$  with  $v = 0, 1, 2, \dots$

The harmonic approximation is in good agreement with observations for small elongations. In reality, the binding potential is anharmonic. Different contributions of repulsion and attraction to the potential have to be considered. The repulsion arises due to the Pauli principle as a result of the overlap of the occupied orbitals, which dominates at short internuclear distances  $R < R_e$ . On the other hand, attraction due to the Coulomb potential is present, which dominates on a long-range scale ( $R > R_e$ ). An empirical description is given by the Morse potential [16]

$$V_M = D_e(1 - \exp(-\beta(R - R_e)))^2. \quad (2.14)$$

$\beta$  is a constant specific to the molecule. The energy required to separate the diatomic molecule, i.e.  $R \rightarrow \infty$  in equation (2.14), is the dissociation energy  $D_e$ . Adapting the Schrödinger equation of the quantum harmonic oscillator by introducing the Morse

potential instead of a parabolic one as in (2.12), finally leads to the vibrational energy

$$G(v) = \omega_e \left( v + \frac{1}{2} \right) - \omega_e \chi_e \left( v + \frac{1}{2} \right)^2, \quad \omega_e = \frac{\beta}{2\pi c} \sqrt{\frac{2D_e}{\mu}}, \quad \chi_e = \frac{hc\omega_e}{4D_e}. \quad (2.15)$$

Here, the constants  $\omega_e$  and  $\chi_e$  have been introduced, which are molecular specific.

### 2.1.3 Rovibrational spectrum

Finally, the total energy including the electronic contribution  $T_{\text{el}}$  and the derived rotational and vibrational contributions is given by [13, 14]:

$$\frac{E}{hc} = T_{\text{el}} + BN^+(N^+ + 1) - D(N^+)^2(N^+ + 1)^2 + \omega_e \left( v + \frac{1}{2} \right) - \omega_e \chi_e \left( v + \frac{1}{2} \right)^2 \quad (2.16)$$

The vibration of NO molecules at room temperature is negligible, i.e.  $v = 0$  [17]. Thus, the vibrational spectrum is not of importance in this work. Nevertheless, it was introduced for completeness.

## 2.2 Couplings of angular momenta

So far, the nuclei's motion has been treated independently from the electronic one. However, it is important to consider the coupling between the rotational and electronic motion in terms of angular momenta in order to describe the molecule's spectrum. For a diatomic molecule, different angular momenta couplings are described in the scope of the Hund's coupling cases. The following section is based on [14, 17].

First of all, the relevant angular momenta are described. The total angular momentum is  $\mathbf{J}$ . It may be introduced in the scope of the model of the vibrating symmetric top, where  $\mathbf{J}$  results from a coupling between the angular momentum perpendicular to the internuclear axis and the angular momentum of an electron cloud along the internuclear axis. However, in the following  $\mathbf{J}$  describes the sum of the relevant angular momenta. The electronic spin angular momentum is  $\mathbf{S}$  and the total angular momentum without the electron spin is  $\mathbf{N}=\mathbf{J}-\mathbf{S}$ . The electronic orbital angular momentum is  $\mathbf{L}$  and the rotational angular momentum of the nuclei is  $\mathbf{N}^+$ . There are five Hund's coupling cases, (a) - (e). For NO, only Hund's cases (a), (b), and (d) are important, thus only these cases are discussed. Figure 2.2.1 illustrates the coupling cases in vector diagrams.

### 2.2.1 Hund's case (a)

A Hund's case (a) is sketched in the top left of figure 2.2.1. One can see, that  $\mathbf{L}$  is coupled to the internuclear axis while  $\mathbf{S}$  is coupled to  $\mathbf{L}$ . The coupling is based on strong electrostatic forces, respectively spin-orbit coupling. One refers to the internuclear axial components of  $\mathbf{L}$  and  $\mathbf{S}$  as  $\Lambda$  and  $\Sigma$ . Their sum is given by  $\Omega = \Lambda + \Sigma$ .  $\mathbf{L}$  and  $\mathbf{S}$  have two opposite senses of precession ( $\pm\Lambda$  and  $\pm\Omega$ ) leading to two degenerate levels. This degeneracy is referred to as  $\Lambda$ -doubling and  $\Omega$ -doubling and can be lifted. The further vector couplings can be seen in the diagram. Good quantum numbers, which are a conserved quantity, form a basis and diagonalize the Hamiltonian. In this case, good quantum numbers are  $\Lambda, S, \Sigma, J, M_J$ .  $M_J$  is the component of  $\mathbf{J}$  in a space-fixed  $z$ -direction. Hund's case (a) is considered to be a good description of the coupling situation if  $A\Lambda \gg BJ$ , where  $A$  is the spin-orbit coupling constant, and  $B$  is the rotational constant. This condition is only fulfilled for low  $J$ . [14]

### 2.2.2 Hund's case (b)

A Hund's case (b) is depicted on the top right of figure 2.2.1. In contrast to Hund's case (a), there is no or very weak coupling of  $\mathbf{S}$  to the internuclear axis due to weak spin-orbit coupling. Here,  $BJ \gg A\Lambda$  holds true. Consequently,  $\Sigma$  and  $\Omega$  are not good quantum numbers, as they are in case (a). The good quantum numbers in Hund's case (b) are  $\Lambda, S, N, J, M_J$ . For non-Rydberg states, Hund's case (a) and (b) are the most common in diatomic molecules. [14]

### 2.2.3 Hund's case (d)

Hund's case (d) is important when dealing with Rydberg states of molecules such as NO, as it represents the case where the interaction between the highly excited electron and the ionic core is very weak. Thus, the description of the rotational energy as given in equation (2.8) is valid. The vector couplings are shown in the bottom part of figure 2.2.1,  $\mathbf{N}^+$  is coupled to  $\mathbf{L}$ , resulting in the angular momentum  $\mathbf{N}$ . In turn,  $\mathbf{N}$  and  $\mathbf{S}$  couple to  $\mathbf{J}$ . Due to the fact that  $\mathbf{L}$  is not coupled to the internuclear axis anymore, the transition from Hund's case (b) to (d) is referred to as  $\mathbf{L}$  uncoupling [17]. Good quantum numbers are  $L, S, N^+, N, J, M_J$ .

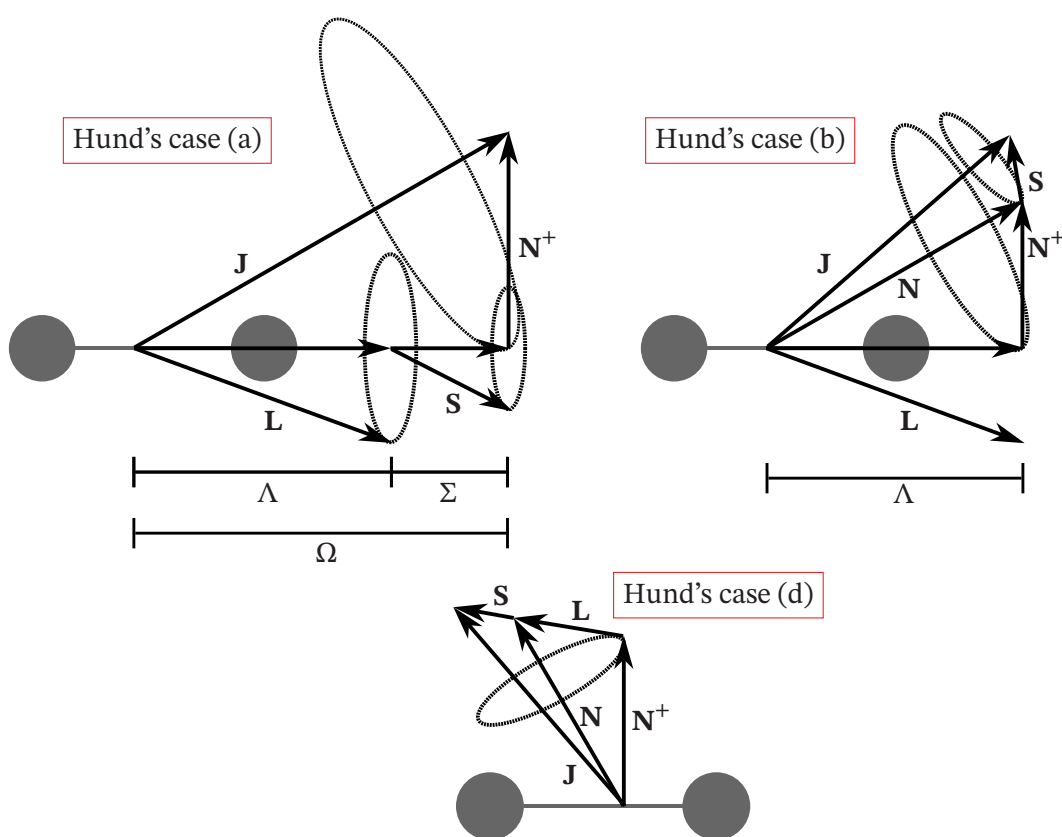


**Figure 2.2.1:** The Hund's cases (a), (b), and (d) which are relevant for the description of NO, are illustrated in vector coupling diagrams. The figure is based on [14].

### 2.3 Excitation of NO

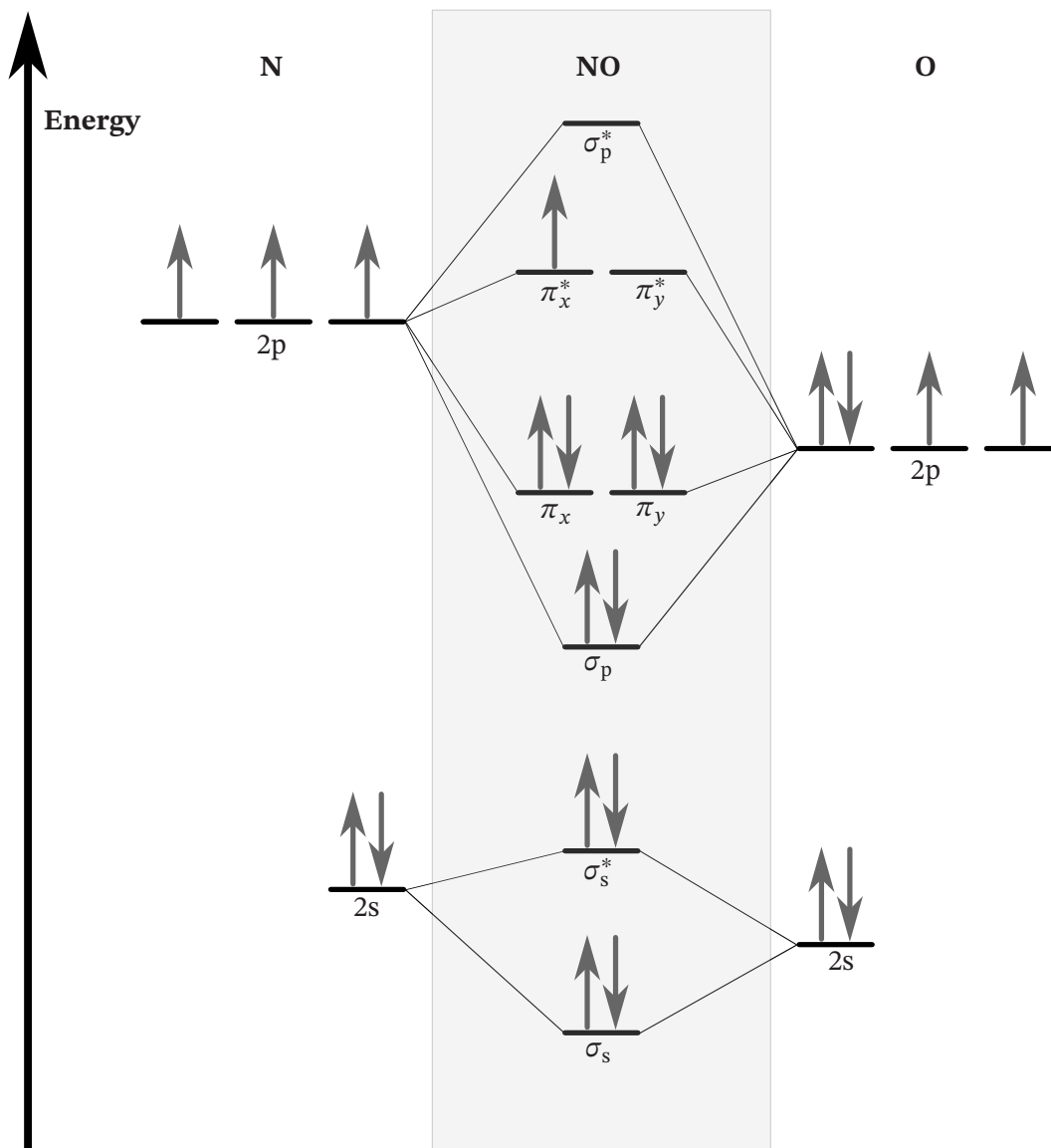


**Figure 2.3.1:** The molecular orbital diagram of the ground state of NO is shown. On the left and right hand side are the atomic orbitals of nitrogen (N) and oxygen (O). The figure is based on [18].

The previous sections introduced the rotational and vibrational structure, as well as different angular coupling cases relevant to the description of NO. Now, the electronic structure is considered. At first, we look at the molecular orbital diagram of the ground state of NO in figure 2.3.1. It is important to note, that there is a single valence electron

sitting in the antibinding  $\pi_x^*$ -orbital ( $\pi_{2p}^*$ ). This is the electron that is excited to a Rydberg state. This is in contrast to nitrogen ( $N_2$ ), which will be important for the discussion later on. Here, the  $\pi_x^*$  orbital is not occupied.

### 2.3.1 Labeling of a molecular state

Before heading to the excitation scheme, a short insight is given on the labeling of a molecular state based on [13, 17].

One may label a state in two different ways. The first one is to consider the electronic configuration. The labeling is done in the notation  $nl\lambda^x$ .  $n$  is the principal quantum number, and  $l$  is the angular momentum quantum number of the atomic orbital. The labels of the molecular orbitals add an extra Greek letter  $\lambda$  which determines the basic shape of the molecular orbital analogous to  $l$  for an atomic orbital. A \*-sign is added if the orbital is antibonding, which means that the atomic wavefunctions overlap in a destructive way. The exponent  $x$  states the number of electrons in the orbital.  $\lambda = 0, 1, 2, \dots$  orbitals are called  $\sigma, \pi, \delta, \dots$  and  $l = 0, 1, 2, \dots$  is referred to as s, p, d, ... Thus, the electronic configuration of the ground state NO is  $(1s\sigma)^2(1s\sigma^*)^2(2s\sigma)^2(2s\sigma^*)^2(2p\pi)^4(2p\pi^*)^1$ .

Labeling a molecular state is done in the notation

$$X^{2S+1}\Lambda_{\Omega}^{\pm}. \quad (2.17)$$

$\Omega$  is only assigned in Hund's case (a), not in (b) and (d). It is important to note that the ground state is usually labeled as «X». The following states are labeled in the order of the alphabet. If a new state was discovered in between two states e.g. between the states A and B, the latest discovered state will be labeled A'.  $\Lambda$  and  $\Omega$  have already been introduced in the previous section.  $S$  describes the total electron spin and  $2S + 1$  is the multiplicity. The exponent of  $\Lambda$  indicates the parity: + means, that the wavefunction is symmetric when mirroring at a plane perpendicular to the internuclear axis, – describes the contrary case.

It is appropriate to describe the ground state  $X^2\Pi$  of NO as a Hund's case (a) for low  $J$  [19]. Due to the single electron in the  $\pi_{2p}^*$  orbital the total spin  $S$  is  $S = 1/2$ . Consequently,  $\Sigma = \pm 1/2$  and  $\Lambda = \pm 1$ . As  $\Omega = |\Lambda + \Sigma|$  holds, there are two values possible, i.e.  $\Omega = 1/2$  and  $\Omega = 3/2$ .

Thus, NO has two distinct states arising from spin-orbit coupling, namely  $X^2\Pi_{3/2}$  and  $X^2\Pi_{1/2}$ . Since the splitting between the states is small and their population at room temperature is quite similar, the  $X^2\Pi_{3/2}$  state has been chosen for the experimental investigations because there is more information available on the subsequent transitions in the excitation scheme [20].

### 2.3.2 Rydberg states

In the experiment, ground state molecules of NO are excited into a Rydberg state. The latter one is a highly excited electronic state, where the electron has a high principal quantum number  $n$ , and is thus, on average, comparably far away from the nucleus [21]. A small insight is given here, based on the hydrogenic energy level structure [22].

Since hydrogen consists only of one proton and one electron the calculation of the energy levels of the valence electron is quite simple in comparison to particles with more electrons or even more cores. According to the Planck postulate, the energy levels are quantized. The energy levels in hydrogen are given by the Rydberg formula

$$E_n = -\frac{E_R}{n^2}. \quad (2.18)$$

The Rydberg constant for hydrogen is  $E_R \approx 13.6$  eV,  $n$  is the principal quantum number.

Alkali atoms are the most similar to hydrogen, as they have also a single free valence electron, besides the additional electrons in the closed shells. For a big distance  $r$  of the valence electron to the ionic core, the potential can be described by a Coulomb potential like in hydrogen

$$\lim_{r \rightarrow \infty} V(r) = -\frac{e}{4\pi\epsilon_0 r}. \quad (2.19)$$

The nuclear charge is screened by the inner electrons, making the potential hydrogen-like as the valence electron is effectively interacting with a single positive charge.  $\epsilon_0$  is the vacuum permittivity and  $e$  the elementary charge. In the other case, if  $r \rightarrow 0$ , the valence electron of the alkali atom experiences the full nuclear charge  $Ze$ , instead of  $1 \cdot e$  as in (2.19), with  $Z$  being the number of protons i.e. the nuclear charge number. The probability of the valence electron being near the core decreases for higher principal quantum numbers  $n$  and higher angular quantum numbers  $l$ . To account for the situation of a changed potential and energy decrease at a finite valence electron distance to the core, the Rydberg formula (2.18) can be adapted by introducing an effective principal quantum number  $n_{\text{eff}}$  leading to

$$E_{nl} = -\frac{Ry}{n_{\text{eff}}^2}, \quad n_{\text{eff}} = n - \delta_{nl}, \quad Ry = \frac{\mu e^4}{8\epsilon_0^2 h^2}. \quad (2.20)$$

Here, the quantum defect  $\delta_{nl}$  has been introduced. As noted in the index, it depends on the quantum numbers  $n$  and  $l$  in this case.  $Ry$  is the Rydberg constant, it is proportional to the atom's reduced mass  $\mu$ .

Basically, this description also holds for Rydberg molecules like NO, where the outer electron is excited to a Rydberg state. The Rydberg state of NO is properly described in Hund's case (d) [10, 23]. Nevertheless one has to consider, that the Rydberg electron has a small probability of being near the ionic core. Therefore, the quantum defects are typically described in Hund's case (b) in the first place. The quantum defect reads  $\delta_{l\Lambda}^{(b)}$ .

The known values are listed in table 2.3.1. One may convert the Hund's case (b) to a Hund's case (d) description by a frame transformation, then the quantum defect is  $\delta_{lN^+}^{(d)}$  [23]. The index indicates the appropriate quantum numbers. A mathematical description of the Rydberg states in NO can be done by using a matrix diagonalization approach with additional corrections from multi-channel quantum defect theory (MQDT), which will be not introduced here.

**Table 2.3.1:** Hund's case (b) quantum defects  $\delta_{l\Lambda}^{(b)}$  of NO taken from [24].

		$\Lambda$			
		0	1	2	3
$l$	0	0.210			
	1	0.7038	0.7410		
	2	0.05	-0.053	0.089	
	3	0.0182	0.0172	0.0128	0.0057

Rydberg particles have some special properties. Their dependence on the principal quantum number  $n$  is given in the following [17]:

$$\begin{aligned}
 &\text{Binding energy} \propto n^{-2}, \\
 &\text{Energy spacing between two states} \propto n^{-3}, \\
 &\text{Orbital radius} \propto n^2, \\
 &\text{Polarizability} \propto n^7, \\
 &\text{Dipole moment} \propto n^2, \\
 &\text{Radiative lifetime} \propto n^3.
 \end{aligned}$$

The Rydberg state of NO is  $nl(N^+) X^+ {}^1\Sigma^+$ . This can be attributed by considering the ground electronic state of the nitrosyl cation  $\text{NO}^+$ , which is the ionic core of NO. This has been done in [25]. The + sign in the exponent of the ground state X indicates the positive charge of the NO ion.  $N^+$  is a good quantum number in Hund's case (d) and  $n$  is the Rydberg electron's principal quantum number. Therefore, the Rydberg states in the scope of this work are described as  $n(N^+)$  like in [20]. Other descriptions, e.g. in [23], include the quantum number  $l$ .

### 2.3.3 Labeling and excitation scheme of NO

The excitation scheme of NO is based on selection rules. They can be deduced from the transition dipole moment which is non-vanishing if the particular excitation is possible. There are many different selection rules, however, only the selection rules and labeling

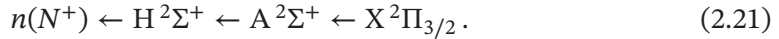
relevant to understanding the excitation scheme will be introduced. Note, that we are considering a heteronuclear molecule here.

The parity may be labeled as described in [26]. In the case of molecules with an odd number of electrons like NO, the convention is that levels with parity  $+(-1)^{J-0.5}$  are e levels and levels with parity  $-(-1)^{J-0.5}$  are f levels [26]. The selection rules are  $e \leftrightarrow f$  if  $\Delta J = 0$  and  $e \leftrightarrow e$  or  $f \leftrightarrow f$  if  $\Delta J = \pm 1$ . Note, that the parity may also be given as + or - as introduced before. Here,  $+ \leftrightarrow -$  holds.

An excitation where  $\Delta J = 0$ , i.e. the quantum number  $J$  does not change is referred to as Q branch. Excitation on the rotational branch P changes the quantum number  $J$  by  $\Delta J = -1$ , while an R branch leads to  $\Delta J = +1$ . Note, that  $\Delta J = J - J'$  where  $J$  is the final and  $J'$  is the initial state.

Furthermore, it is important to introduce the  $F_i$  labeling. Levels with the same quantum number  $N$  may have different  $J$  quantum numbers which results in a splitting which is referred to as spin-rotation splitting. The level with lower energy is the  $F_1(J)$  series, the series with higher energy is  $F_2(J)$ . In Hund's case (b) and for  $S = 1/2$  the following holds:  $J = N + 1/2$  in case of the  $F_1(J)$  series and in the other case  $J = N - 1/2$  which is the  $F_2(J)$  series [14].

In this work, NO is excited to a Rydberg state by a three-photon excitation path using continuous-wave (cw) laser systems. The excitation path is given in (2.21), where the ground state is on the right and the final state on the left hand side



This convention is common in molecular physics and has also been established in publications of this project's group [20, 27].

Starting from the ground state  $\text{X}^2\Pi_{3/2}$ , which has been introduced in subsection 2.3.1, NO is excited to the  $\text{A}^2\Sigma^+$  state. The transition wavelength is at around 226 nm, which is in the ultraviolet (UV) range of the electromagnetic spectrum [28]. The  $\text{A}^2\Sigma^+$  state is described in a Hund's case (b) [29].

Next, we excite to the  $\text{H}^2\Sigma^+$  state. The  $l$ -character of this state indicates the possible  $l$  quantum number of the Rydberg states as the transitions are in principle based on selection rules. The  $\text{H}^2\Sigma^+$  state has 38 % s-character ( $l = 0$ ) and 62 % d-character ( $l = 2$ ), and is described best as Hund's case (b) [30]. The transition wavelength is at 540 nm, thus in the green wavelength regime [31].

According to [17, 23],  $\Delta l = \pm 1$  holds. Thus, the Rydberg states have predominantly quantum numbers  $l = 1, 3$  (p and f). We expect to see f-states as p-states dissociate fast [23]. However, the selection rules are not strict due to the molecule's complexity. The final transition is the transition to a Rydberg state  $n(N^+)$ , which has already been discussed in the previous section. The Rydberg transition wavelength is between 835 nm

and 850 nm, thus in the infrared regime. An explanation, of how the transition wavelengths are determined will be given in the next chapter. The accessible rotational series with quantum numbers  $N^+$  depend on the rotational branches chosen for the lower transitions.

A short insight into the excitation scheme of NO is given in the following. The excitation scheme of NO reproduced after [20] is shown in figure 2.3.2. The explanations are based on [17]. For lower states apostrophes in the exponent of the quantum numbers are added.

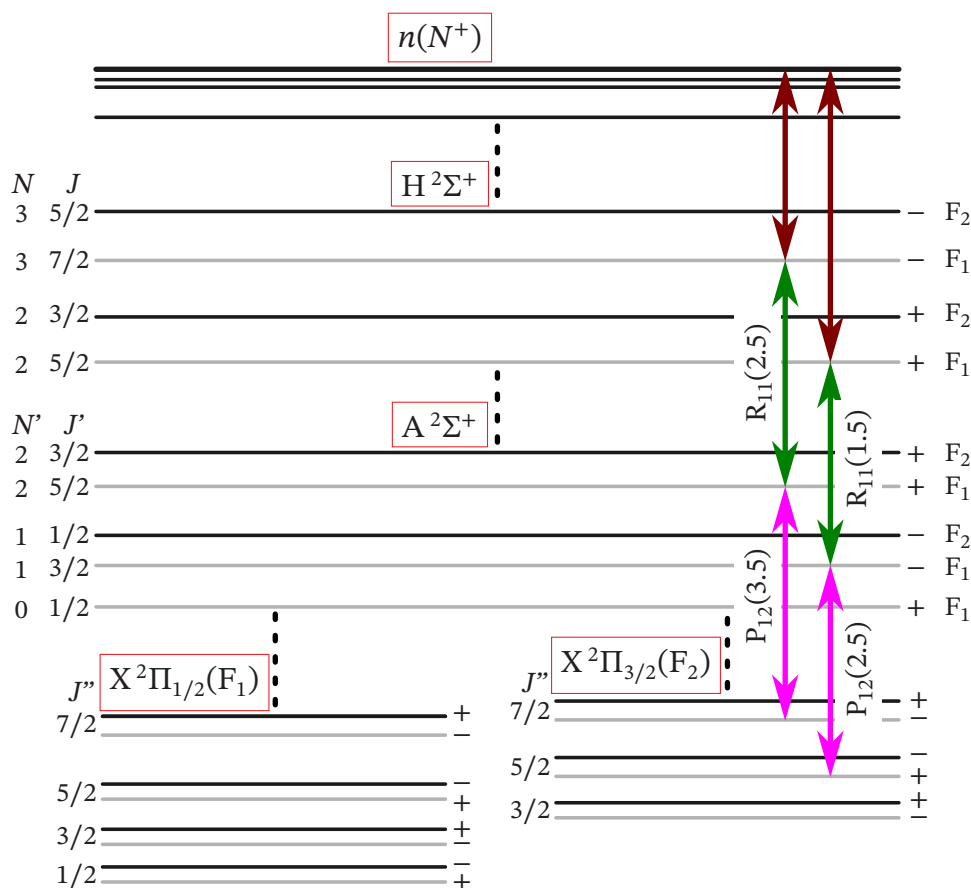


**Figure 2.3.2:** The excitation scheme of NO including substructures is shown. The ground (X), intermediate (A, H) and the Rydberg state ( $n(N^+)$ ) are labeled. Light and dark colors indicate e and f parity. The parity is also indicated by the + and - sign. Two excitation paths following the selection rules, leading to the excitation of the  $N^+ = 0, 2$  series (right one), and the  $N^+ = 1, 3$  series (left one) are sketched. The excitation scheme has been reproduced based on [20], which is in turn based on [31–33].

The rotational branches in the figure are labeled considering  $\Delta J$ ,  $F_i$  and the initial quantum number  $J$ . Thus,  $P_{12}(2.5)$  means, that  $\Delta J = -1$ , the initial  $J = 2.5$ , and  $F_i$  changes from  $F_1$  to  $F_2$ . The symmetry is described by the + and - sign, and the lighter color of the lines represents parity e and the darker color is f, respectively.

The rotational branches of the two different excitation paths, depicted in figure 2.3.2, allow the excitation to different Rydberg series. A simplified explanation for the accessible  $N^+$  accounting for the Hund's cases, selection rules, and the state's  $l$ -character is given here. If the branches  $P_{12}(2.5)$  for the first and  $R_{11}(1.5)$  for the second transition are chosen, the second intermediate state  $H^2\Sigma^+$  has the quantum number  $N = 2$ . For the Rydberg state,  $N = N^+ + l \Leftrightarrow N^+ = N - l$  holds. As already stated, the  $H^2\Sigma^+$  state has dominantly  $l = 0, 2$ . Thus,  $N^+ = 0$  and  $N^+ = 2$  are accessible by this excitation path. Choosing the rotational branches  $P_{12}(3.5)$  and  $R_{11}(2.5)$  leads to other two accessible rotational series, namely  $N^+ = 1, 3$ . The knowledge about the excitation path is important to understand which states can be excited.

## 2.4 Spectroscopic line broadening and shifts

### 2.4.1 Line shapes

Spectroscopic lines are not infinitely thin. Instead, different mechanisms contribute to a line broadening. Moreover, a shift of the line can be observed. This section is based on [34–36]. The width of the spectroscopic line is quantified by the parameter  $\Delta\omega$ , which gives the full width at half maximum (FWHM) of the line.

Basically, one differentiates between two types of broadening. Homogeneous broadening leads to a Lorentzian lineshape, inhomogeneous broadening typically results in a Gaussian profile. While in the first case, all individual particles would lead to the same spectrum, in the latter case, the particles in the system behave differently, which means that the emission and absorption rate at a certain frequency  $\omega$  is different for the individual particles.

The intensity profile in the case of homogeneous broadening is

$$I_L(\omega) = \frac{L}{(\omega - \omega_0)^2 + \left(\frac{\Delta\omega_L}{2}\right)^2}. \quad (2.22)$$

By choosing  $L = \Delta\omega_L/2\pi$  the intensity profile is normalized such that  $\int_0^\infty I_L(\omega) d\omega = 1$ .  $\Delta\omega_L$  is the FWHM of the Lorentzian lineshape.

The description of a Gaussian profile is

$$I_G(\omega) = G \exp\left(-\frac{(\omega - \omega_0)^2}{2\sigma^2}\right). \quad (2.23)$$

Area normalization is done by choosing  $G = 1/\sqrt{2\pi}\sigma$ . The actual FWHM of the Gaussian lineshape is  $\Delta\omega_G = 2\sqrt{2 \ln 2}\sigma$ .

Oftentimes, if different types of broadening mechanisms contribute to the overall linewidth, a proper description of the lineshape is a Voigt profile which is the convolution of a Gaussian and Lorentzian profile, i.e.

$$I_V(\omega) = (I_G * I_L)(\omega). \quad (2.24)$$

The linewidth of the Voigt profile to high precision is given by [37]

$$\Delta\omega_V \approx \frac{1}{2} \left( 0.5346(\Delta\omega_L) + \sqrt{0.2165975 (\Delta\omega_L)^2 + 4(\Delta\omega_G)^2} \right). \quad (2.25)$$

### 2.4.2 Broadening mechanisms

Now, different broadening mechanisms are introduced. An excited state has a radiative lifetime  $\tau$ . This is the time the electron is in the excited state, before dropping to a lower one while emitting light. Basically, for atoms, it can be calculated using Einstein coefficients. Using the time–energy uncertainty relation  $\Delta E\tau \gtrsim \hbar$  and  $\Delta\omega \propto \tau^{-1}$  leads to the natural linewidth,

$$\Delta\omega_{\text{life}} = \frac{\Delta E}{\hbar} \gtrsim \frac{1}{\tau}. \quad (2.26)$$

The natural broadening is homogeneous.

Particles in a system of finite temperature perform a random motion which is referred to as a Brownian motion. We assign  $\omega_0$  as the transition frequency between the ground and excited state in the rest frame of the particle. If we suppose that the particle is moving on the  $x$ -axis with velocity  $v_x$ , the actual frequency  $\omega$  detected by an observer is not  $\omega_0$ , but

$$\omega = \omega_0 \left( 1 \pm \frac{v_x}{c} \right) = \omega_0 \pm kv_x. \quad (2.27)$$

The magnitude of the wavevector is  $k = \omega_0/c$ . If the particle is moving towards the observer the  $+$  sign accounts for this situation and the frequency observed is  $\omega > \omega_0$ . In the other case of a particle moving away,  $\omega_0 < \omega$  holds. This is referred to as the Doppler effect. The velocity distribution which describes the amount of particles  $N$  at a certain velocity  $v_x$  is a Maxwell-Boltzmann distribution

$$N(v_x) = N_0 \left( \frac{2k_B T}{\pi m} \right)^{\frac{1}{2}} \exp\left( -\frac{mv_x^2}{2k_B T} \right), \quad (2.28)$$

where  $N_0$  is the total amount of particles,  $m$  their corresponding mass and  $T$  the temperature. This leads to a Gaussian broadening with FWHM

$$\Delta\omega_{\text{Doppler}} = 2\omega_0 \left( \frac{(2\ln 2)k_B T}{mc^2} \right)^{\frac{1}{2}}. \quad (2.29)$$

Supposing that particles are moving perpendicularly to the laser beam, the interaction time between the particle and the exciting laser beam is given by the transit time

$$t_{\text{transit}} = d/v_z. \quad (2.30)$$

Here,  $d$  is the beam diameter and  $v_z$  is the particle velocity perpendicularly to the beam. Taking into account the Maxwell-Boltzmann distribution of velocity one can deduce the FWHM of

$$\Delta\omega_{\text{transit}} = \left( \frac{96k_B T \ln 2}{md^2} \right)^{\frac{1}{2}}. \quad (2.31)$$

If the transit-time  $t_{\text{transit}}$  is shorter than the radiative lifetime  $\tau$ , the main contribution to the linewidth is not  $\tau$  but  $t_{\text{transit}}$ .

Power broadening is homogeneous and occurs due to saturation in the absorption. Above the saturation intensity  $I_{\text{sat}}$ , contributions of power broadening to the line shape become significantly dominating. The FWHM is given by

$$\Delta\omega_{\text{power}} = \Delta\omega_{\text{life}} \left(1 + \frac{I}{I_{\text{sat}}}\right)^{\frac{1}{2}}. \quad (2.32)$$

Also, the absorption and thus the peak value of the spectroscopic line at  $\omega_0$  is decreased.

The broadening mechanism of main interest in the scope of this work is pressure broadening. Basically, this can be explained by the fact that the energy levels of the particles shift due to the collisional interaction between two particles. The FWHM is given by

$$\Delta\omega_{\text{collision}} = N\sigma\bar{v}, \quad \bar{v} = \left(\frac{8k_B T}{\pi\mu}\right)^{\frac{1}{2}}. \quad (2.33)$$

The particle density is  $N$ ,  $\sigma$  is the collisional broadening cross section and the mean relative velocity between the collisional partners is  $\bar{v}$ . The reduced mass of the collisional partners is  $\mu$ . In the case of a Rydberg particle, i.e. a Rydberg atom or molecule interacting with a collisional partner, which is referred to as the perturber, the collisional cross section has three main contributions and is in total given by [38]

$$\sigma = \frac{1}{2}(\sigma_{\text{el}} + \sigma_{\text{inel}} + \sigma_{\text{ion}}). \quad (2.34)$$

Here, only the Rydberg state and not the ground state contributes to the cross section, thus the factor  $1/2$  is introduced. The elastic scattering broadening cross section between the Rydberg electron and the perturber is  $\sigma_{\text{el}}$  and  $\sigma_{\text{inel}}$  is the inelastic, respectively. The collision between the Rydberg ion and the perturber is described by  $\sigma_{\text{ion}}$ . Further details are given in the next section.

### 2.4.3 Collisional shift and broadening

This section is strongly based on [38]. Concerning Rydberg particles, one may distinguish two categories of collisional interaction. In the first case, the perturber is interacting with the whole Rydberg particle. This is true for a long-range interaction. An example is a charge-dipole interaction of the Rydberg particle with an ionic one, or a dipole-dipole interaction of the Rydberg particle with another polar particle. This may be the case if a NO molecule in a Rydberg state is interacting with another NO particle. The charge-dipole interaction scales with  $V \propto r^{-2}$ , for the dipole-dipole interaction  $V \propto r^{-3}$  holds. The internuclear distance between the Rydberg particle and the perturber is  $r$ , and  $V$  the potential describing their interaction.

The other category of collisional interaction is of a shorter range. This is the case if the perturber is a neutrally charged, non-polar molecule like  $N_2$ . The Rydberg-perturber interaction is a dipole-induced dipole interaction scaling with  $V \propto r^{-6}$ , which is in this case the longest range interaction [38]. Due to the scaling of the potential, it only becomes significant for small distances  $r$  between the collisional partners. An individual interaction between the perturber  $N_2$  and the Rydberg electron respectively the Rydberg ion core is possible [38].

Another differentiation can be done between elastic and inelastic collisions. In the case of elastic collisions, the kinetic energy is preserved. Elastic collisions lead to a kinetic energy exchange and not an exchange of inner energy between the collisional partners as is the case for inelastic collisions. If e.g. the perturber is a ground state rare gas atom, there are no available states due to the fact that their shells are fully occupied by the electrons. Thus, scattering with the Rydberg electron is elastic. The kinetic energy exchange is approximately given by [17]

$$\Delta E = 4k_B T \frac{v}{V}. \quad (2.35)$$

The velocity of the Rydberg electron is  $v$ , the relative velocity of the rare gas atom and Rydberg particle is  $V$ .

The situation becomes more complicated if the perturber is a molecule. Despite fully occupied molecular orbitals like in  $N_2$ , an inner energy exchange between the Rydberg electron and the perturber may occur. Here, the Rydberg electron can lead to vibrational or quadrupole-induced rotational transitions in the molecule by a resonant energy exchange. Consequently, the state of the Rydberg electron changes as well, ionization is also possible. This kind of collisional interaction is referred to as inelastic scattering.

While both elastic and inelastic collisions contribute to a broadening of the line, only elastic collisions may lead to a line shift. This effect was first measured by Amaldi and Segrè [39]. They observed a pressure-dependent shift of the spectroscopic line in the alkaline sodium interacting with the perturber gas hydrogen and recognized that the shift is nearly proportional to the concentration of the perturber gas. An explanation for this observation has been given by Fermi [7].

The following discussion is based on [17, 40, 41]. The total energy shift  $\delta$  due to elastic collisions contains two contributions

$$\delta = \delta_{el} + \delta_{ion}. \quad (2.36)$$

The first contribution  $\delta_{el}$  relies on the elastic scattering of the Rydberg electron and the perturber. The Rydberg ion and perturber interaction is given by  $\delta_{ion}$ . The latter one is based on polarization effects due to a dielectric screening of the Rydberg electron by the perturber. Thus, the effect depends on the dielectric properties of the perturber. However, it is small compared to the contribution  $\delta_{el}$ . The overall result in Fermi's paper

leads to the following density dependencies of the shifts:

$$\delta_{\text{el}} \propto N, \quad (2.37)$$

$$\delta_{\text{ion}} \propto N^{\frac{1}{3}}. \quad (2.38)$$

The linear density dependency arising from the Rydberg electron-perturber scattering is characteristically found in the impact regime [17]. Therefore, a brief overview of the derivation based on [7, 40] is given, leading to the so-called Fermi shift. First of all, the Schrödinger equation, including two different potentials is set up

$$\left( -\frac{\hbar^2}{2m} \nabla^2 + U + \sum_i V_i \right) \psi = E\psi. \quad (2.39)$$

The first term describes the kinetic energy of the Rydberg electron with mass  $m$ . The potential  $U$  is the Coulomb interaction between the Rydberg electron and the ionic core. The potentials  $V_i$  are based on the interaction of the Rydberg electron with the perturber particles.  $V_i$  has a dominant contribution to the electron's wavefunction only at small distances between the perturber and the electron leading to irregularities of the wavefunction  $\psi$ . The potential  $U$  is changing slowly and thus assumed to be constant. Now, the wavefunction  $\bar{\psi}$  is introduced, which is an averaged wavefunction in an area small when compared to the de Broglie wavelength of the electron yet contains a significant amount of perturbers [40]. Now, the Rydberg electron's wavefunction is denoted by  $\bar{\psi}$ , which is regular. The approximation regarding the wavefunction is also explained in figure 2.4.1. The main steps of the calculation as described in [40] are shown. The Schrödinger equation including  $\bar{\psi}$  reads

$$\frac{\hbar^2}{2m} \nabla^2 \bar{\psi} + (E - U) \bar{\psi} - \sum_i V_i \psi = 0. \quad (2.40)$$

Next, one can assign

$$u(r) = (a + r) \bar{\psi} \quad (2.41)$$

with the scattering length  $a$ , leading to approximatively

$$\left( -\frac{\hbar^2}{2m} \right) u''(r) + V(r)u(r) = 0. \quad (2.42)$$

Integration of equation (2.42) and considering equation (2.41) leads to

$$\left( \frac{2m}{\hbar^2} \right) \bar{V} \bar{\psi} = -4\pi a \bar{\psi}. \quad (2.43)$$

Now, one may replace the last term in equation (2.40) by

$$\sum_i V_i \psi = -\frac{2\hbar^2 \pi a N}{m} \psi, \quad (2.44)$$

finally leading to the linear energy shift  $\delta_{\text{el}}$ :

$$\delta_{\text{el}} = \frac{2\hbar^2 \pi a}{m} N \quad (2.45)$$

In the case of  $a > 0$  a blue shift occurs. This is the case for dominantly repulsive interaction. In the other case,  $a < 0$  and a red shift of the spectroscopic line is observed.

Basically, what happened here, is an induced phase-shift of the Rydberg electron's wavefunction due to the elastic scattering of the Rydberg electron and a perturber resulting in a linear shift of the spectroscopic line.

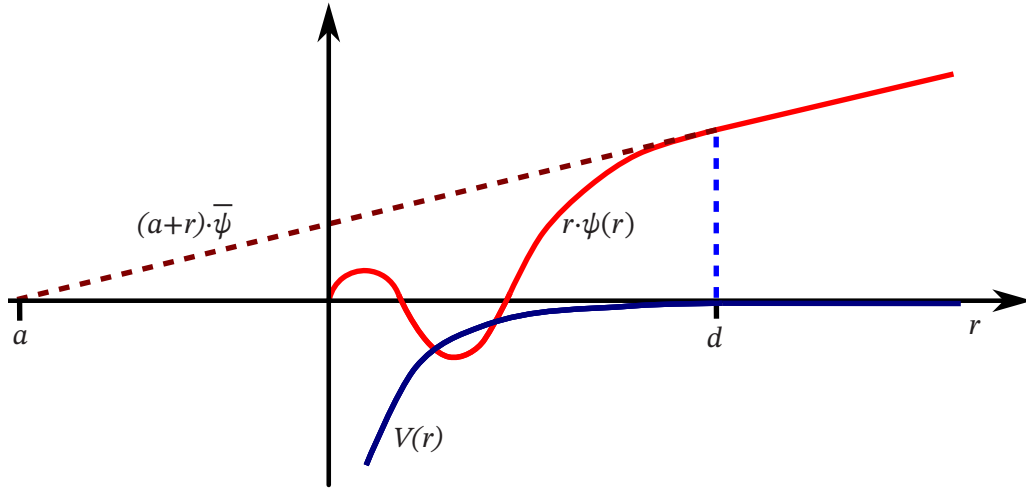


**Figure 2.4.1:** Illustration of the wavefunction  $r\psi(r)$  of the Rydberg electron (red) and the interaction potential (blue) between the Rydberg electron and perturber  $V(r)$ . For  $r > d$  the potential  $V(r)$  is very small and it is justified to introduce the linear wavefunction  $u(r) = (a + r)\bar{\psi}$  (see equation (2.41)) with the constant  $\bar{\psi}$  as has been done by Fermi. The scattering length  $a$  is also indicated in the figure. The illustration is based on [7, 20].

## 2.5 Stark effect

The Stark effect describes the splitting and shift of energy levels caused by an electric field. Quantum mechanically, it is based on the coupling of the dipole operator  $\mathbf{d}$  with the electric field  $\mathbf{F}$ .

A calculation leading to the linear and quadratic Stark effect can be done using time-independent perturbation theory. The derivation follows the explanation in [42], which is based on the atomic Stark effect but can in principle be extended to molecules for qualitative understanding. One starts by assuming a static and homogeneous electric field along the  $z$ -axis. Thus, the electric field  $\mathbf{F} = (0, 0, -F_z)^T$ , has only a component in the  $z$ -direction leading to the scalar potential

$$\phi(\mathbf{r}) = -F_z z. \quad (2.46)$$

The full Hamiltonian is  $\mathbf{H} = \mathbf{H}_0 + \mathbf{H}_1$ . The unperturbed Hamiltonian is  $\mathbf{H}_0$ , whereas  $\mathbf{H}_1$  is the perturbation due to the electric field given by

$$\mathbf{H}_1 = -e \sum_{i=1}^A \phi(\mathbf{r}_i) = eF_z \sum_{i=1}^A z_i. \quad (2.47)$$

Here, an atom with  $A$  electrons is considered. Time-independent perturbation theory in first order leads to

$$\Delta E_n^{(1)} = eF_z \left\langle \Psi_n \left| \sum_{i=1}^A z_i \right| \Psi_n \right\rangle. \quad (2.48)$$

The eigenstates of  $\mathbf{H}_0$  are  $\psi_n$ . One may recognize that the energy shift scales linearly with the electric field, thus this is referred to as the linear Stark effect. The matrix element is non-vanishing if the eigenstates are degenerate. This may be the case in polar particles, which have a permanent dipole moment [43].

The second-order contribution reads

$$\Delta E_n^{(2)} = (eF_z)^2 \sum_{E_m \neq E_n} \frac{\left| \left\langle \Psi_n \left| \sum_{i=1}^A z_i \right| \Psi_m \right\rangle \right|^2}{E_n - E_m}. \quad (2.49)$$

The eigenenergies of the non-degenerate eigenstates  $\psi_n$  and  $\psi_m$  are  $E_n$  and  $E_m$ . The energy shift is quadratically dependent on the electric field, which is referred to as the quadratic Stark effect. One may write equation (2.49) in another way:

$$\Delta E_n^{(2)} = -\frac{\alpha}{2} F_z^2, \quad (2.50)$$

where  $\alpha$  is the dipole polarizability. This indicates the fact, that the quadratic Stark effect occurs due to polarization [43].

A so-called Stark map is a visualization of the Stark effect, A theoretically simulated Stark map of the Rydberg state  $22(0)$  of NO, calculated via matrix diagonalization and MQDT is plotted in figure 2.5.1. This is a common approach in order to include corrections due to the quantum defect. The data is provided by Prof. Stephen Hogan and Dr. Matthew Rayment from the University College London, which are cooperation partners of our group. The  $x$ -axis in figure 2.5.1 shows the electric field  $F$ , while the  $y$ -axis is the energy. It has been converted into a frequency unit that describes the Rydberg laser detuning, similar to the experimental data presented later on. Note, that the detuning is given by the ordinary frequency  $f$  and not the angular frequency  $\omega$ , which are related by  $\omega = 2\pi f$ . The strength of the spectroscopic lines i.e. the character of the state is not included in the plot of the Stark map for clarity.

The  $f$  ( $l = 3$ ) and  $g$  ( $l = 4$ ) state are labeled. High- $l$  states ( $l > 4$ ) are nearly degenerate as can be seen in the figure. As soon as the energy levels approach each other in higher electric fields, the slope of the line changes from a quadratic to a linear behavior. This behavior is indicated with an arrow in the Stark map. The manifold of high- $l$  states, appearing to behave linearly, is referred to as the high- $l$  manifold.

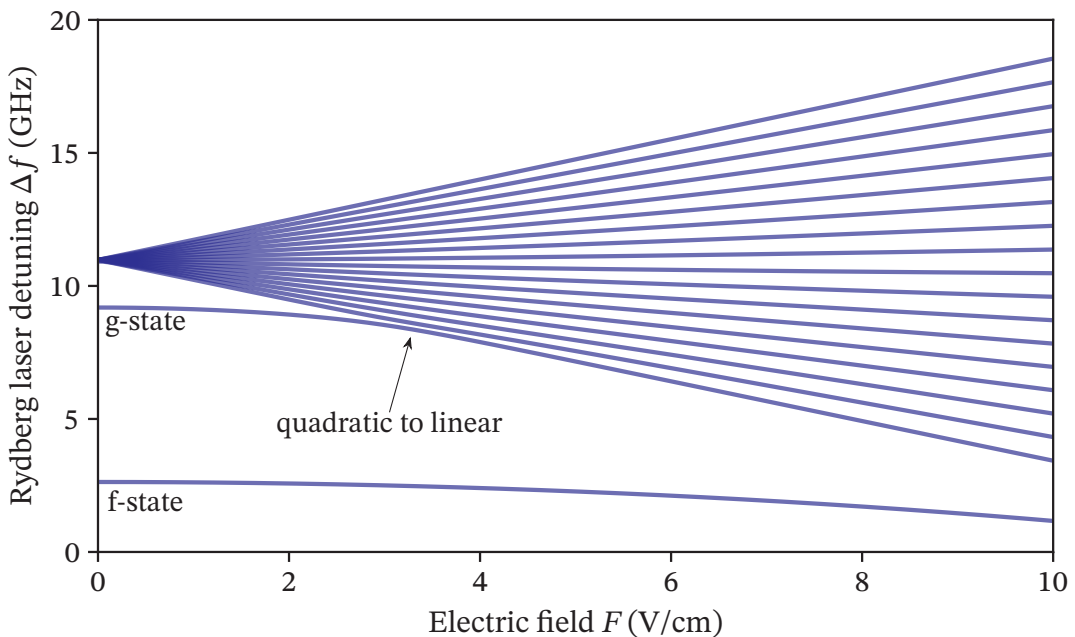


**Figure 2.5.1:** Theoretically simulated Stark map of the Rydberg state  $22(0)$ . The  $f$ - and  $g$ -state are marked. Here,  $M_N = 3$ . The data is provided by our cooperation partners.

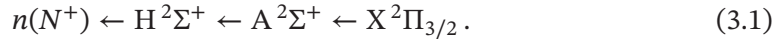
A good quantum number describing the states that are split in the electric field is  $M_N$ . This is the projection of the angular momentum vector  $\mathbf{N}$  to the z-axis in the laboratory frame of reference [23]. For the simulation,  $M_N = 3$  has been chosen. This is the highest reasonable value  $M_N$  can take. Considering the fact that mainly f-states ( $l = 3$ ) are accessible and  $N^+ = 0$ , this leads to  $N = N^+ + l = 3$ .



## 3 Experimental setup and characteristics

### 3.1 Basic working principle

The working principle of the NO trace-gas sensor can be summarized in three main steps. Figure 3.1.1 shows a sketch. In the first step, the gas mixture to be analyzed is directed through the measurement cell. The gas mixture contains either pure NO or a specific mixture of NO diluted in a background gas, in our case N<sub>2</sub>. Next, a three-photon excitation to a Rydberg state using cw laser systems is done inside the cell. The excitation path, as already explained in subsection 2.3.3, is



The transition wavelengths starting from the ground state are in the UV ( $\approx 226$  nm), green ( $\approx 540$  nm), and infrared range (835 nm - 850 nm) of the electromagnetic spectrum. In order to reduce Doppler broadening the UV beam enters the cell counterpropagating towards the other two beams. A frequency stabilization on the UV and green transition is required. Due to noise, a frequency change of the laser light away from the transition frequency occurs and a long-lasting excitation to a Rydberg state will not be possible if the UV and green laser's frequency is not stabilized. The Rydberg laser finally leading to the Rydberg state  $n(N^+)$  is detuned around the wavelength of the Rydberg state chosen. Note, that not all NO molecules inside the cell are excited to a Rydberg state, but only those which are inside the volume where all three laser beams overlap. Following this, collisional ionization inside the cell occurs. The excited NO molecules collide with other particles in the cell, namely other excited or ground state NO molecules, as well as background particles. Thus, the NO molecule is separated into a nitrosyl cation NO<sup>+</sup> and an electron  $e^-$ . The readout of the Rydberg signal is done electronically. The measurement cell, also visible in figure 3.1.2, contains electrodes on the top and the bottom. Applying a voltage yields an electric field inside the cell. Thus, the charges are separated, and guided to the electrodes. A current is generated on the custom-designed printed circuit board (PCB), which is glued on the top of the cell. The currents detected are in the range between some pA to nA. To measure these small currents with an oscilloscope, the electrical circuit on the PCB contains a transimpedance amplifier (TIA), which converts the current into a measurable voltage. Note, that ionization and electrical detection is not limited to the Rydberg state. The intermediate states can also be electrically detected.

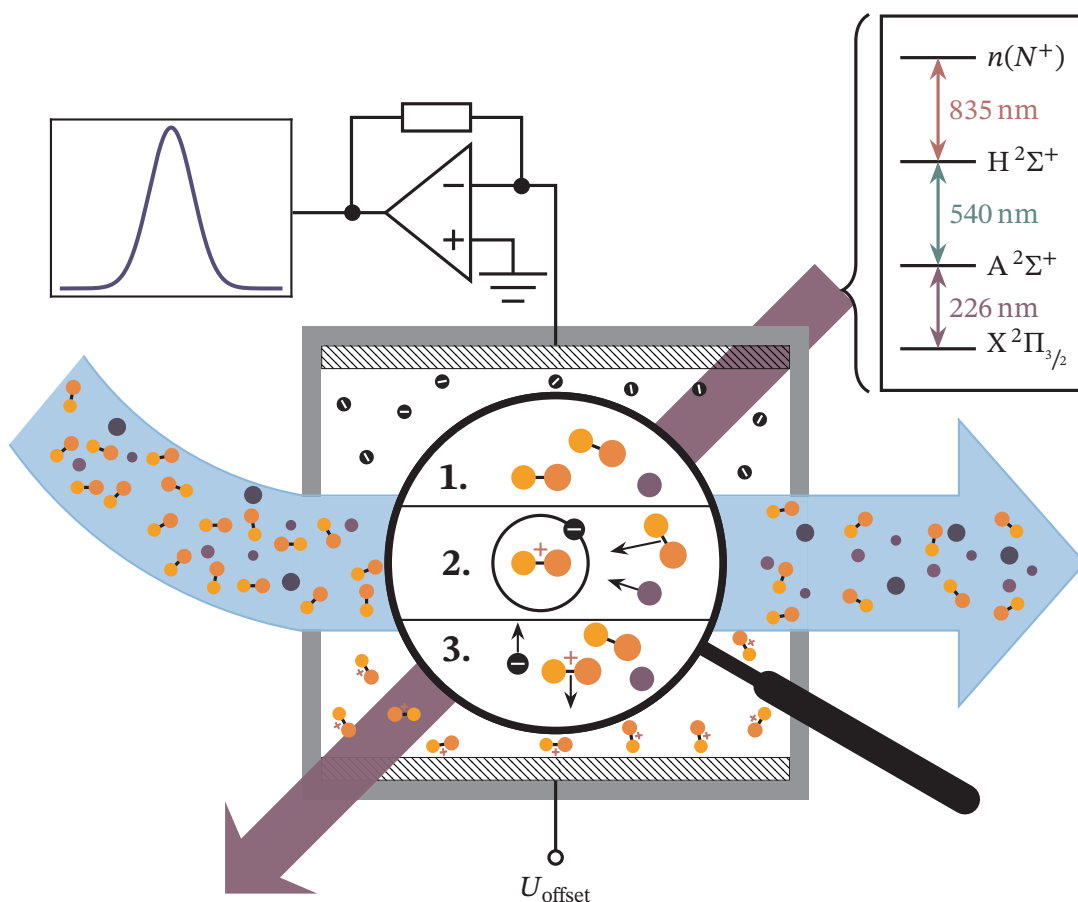


**Figure 3.1.1:** A sketch of the measurement principle is shown, which can be broken down into three main steps. First, a gas mixture containing NO, indicated by a grey arrow, enters the cell. Second, a three-photon excitation to a Rydberg state, as shown in the top right takes place. Collisional ionization leads to a nitrosyl cation  $\text{NO}^+$  and an electron  $e^-$ . By applying a voltage between the electrodes on the top and bottom of the cell, charges are separated and guided to the electrodes. The Rydberg signal is measured with an oscilloscope after conversion of the current to a voltage by a transimpedance amplifier (TIA). The figure has been taken and slightly adapted from [44].

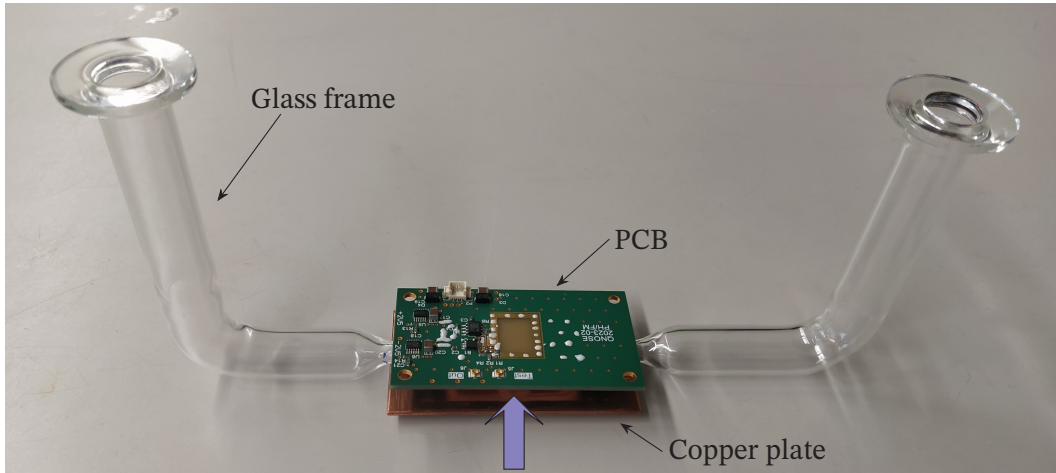


**Figure 3.1.2:** Picture of the through-flow measurement cell. A custom-designed printed circuit board (PCB) (green) is visible, which is glued on top in the middle of the glass frame, including a TIA on its front and an electrode on its back side pointing inside the cell. A copper plate (red) serves as the bottom electrode. The axis of the laser beams is indicated with an arrow. Note, that the UV beam enters the cell counterpropagating towards the other two beams.

One may deduce three main elements from the described working principle of the NO trace-gas sensor. The first element is the laser setup containing the excitation laser systems and the frequency stabilization realized in a separate setup. The second and third elements are the gas mixing unit and the experimental measurement cell. These elements will be introduced in the next sections.

## 3.2 Laser setup

This section describes the experimental and technical background, in particular how the molecular transitions in NO are driven using a special laser setup, including a frequency stabilization of the lasers on the transition frequency. Additionally, an insight into the power stabilization system used for the green and infrared laser beams is given.

### 3.2.1 UV laser system

As mentioned, the ground state transition  $A^2\Sigma^+ \leftarrow X^2\Pi_{3/2}$  requires a wavelength of around 226 nm. The whole UV system has been manufactured by M Squared Lasers. The system is based on a Titan-sapphire (Ti:sa) laser which is used at an emission wavelength of around 904 nm, and an output power of up to 3.5 W. The pump laser is a diode pumped solid state (DPSS) laser with a maximum output power of 18 W at 532 nm. A small fraction of the Ti:sa's output is directed to a wavemeter to readout the wavelength and another fraction is directed to the frequency stabilization setup, which will be introduced later. The remaining power is guided to a so-called doubler, which is a bow-tie ring cavity containing a lithium triborate (LBO) crystal leading to a frequency doubling of the Ti:sa's output, i.e. a wavelength in the range of 452 nm. The output power of the doubler may reach 1.3 W. The output of the doubler is coupled into a quadrupler. The quadrupler consists of a second ring cavity, here a Beta barium borate (BBO) crystal is used for frequency doubling. Finally, UV radiation at 226 nm has been produced by frequency-quadrupling the Ti:sa's emission frequency. The power of the UV beam may reach 50 mW. However, despite regular re-adjustments of the couplings, due to degradation of the pump laser, an output power of 10 mW to 20 mW has been typical during the time of this work, which finally decreased to less than 1 mW. Unlike the other laser beams, in the case of the UV beam, no power stabilization is employed, as the final UV beam power at the cell would become even smaller. The  $1/e^2$  beam waist of the UV laser beam is about 940  $\mu\text{m}$  [20].

### 3.2.2 Green laser system

For the second transition,  $H^2\Sigma^+ \leftarrow A^2\Sigma^+$ , a wavelength of around 540 nm is necessary. Here, a diode laser (Toptica DLPro) is employed. Its output wavelength is at around 1080 nm. Like in the case of the Ti:sa, a small fraction of the output is directed to the wavemeter and the frequency stabilization setup. In order to gain high power after frequency doubling, the diode laser's output is coupled into a ytterbium doped fiber amplifier with a maximum output power of 10 W. Afterwards, a coupling into a periodically poled lithium niobate (PPLN) crystal is done, which doubles the diode laser's frequency to a wavelength of around 540 nm and reaches an output power of up to 1 W. The  $1/e^2$  beam waist of the green laser beam is about 640  $\mu\text{m}$  [20].

### 3.2.3 Infrared laser system

For the final Rydberg transition  $n(N^+) \leftarrow H^2\Sigma^+$  a second Ti:sa system by M Squared is used. Although the experiment has its own infrared laser system based on a diode laser and a tapered amplifier, the infrared Ti:sa system has been used in the scope of this work. The big advantage of the Ti:sa system is its effortless tunability without having to adjust the parameters of the system. The Ti:sa can be tuned in the relevant wavelength range between 835 nm and 850 nm, allowing to excite different Rydberg states  $n(N^+)$ . A big advantage is the possibility to detune the emission frequency periodically in a range of up to 30 GHz. The frequency detuning or scan range is quite stable over time, thus allowing us to measure Stark maps automatically. This will be explained later on in more detail. As for the other laser systems, a small fraction of the laser's radiation is sent to a wavemeter and the frequency stabilization setup. The  $1/e^2$  beam waist of the infrared laser beam is about 1200  $\mu\text{m}$  [20].

### 3.2.4 Power stabilization and regulation

For the laser beam's power stabilization and regulation, as well as modulation, an acousto-optic modulator (AOM) is used for the green and infrared laser beam. Laser modulation, informally referred to as chopping, is necessary for the lock-in technique which will be introduced later.

An insight into an AOM's working principle based on [45, 46] in regard to the experimental setup is given here. As the name already suggests, the operation of an acousto-optic modulator is based on an interaction between sound and light waves. This takes place inside a transparent medium. The refractive index of the medium may be changed due to stress periodically varied by a piezoelectric transducer producing acoustic waves. This is referred to as the elasto-optical effect, leading to a moving phase grating. This optical grating diffracts the incident light in different directions. The fraction of the light  $I_1$  diffracted in the first order, relative to the incident laser beam intensity  $I$  is given by [45]

$$\frac{I_1}{I} = \sin^2 \frac{\Delta\phi}{2}. \quad (3.2)$$

The change in phase is  $\Delta\phi = kL\Delta n$ , where  $k$  is the magnitude of the wavevector and  $L$  is the light-sound interaction length. The change of the refractive index  $\Delta n$  is proportional to the sound wave's amplitude [45]. Following this working principle, one can vary the power transmitted in the zero mode through amplitude modulation based on the piezoelectric transducer. An illustration of the power stabilization setup is visible in figure 3.2.1. To filter out higher-order modes in the experiment, a pinhole is installed right after the AOM. A small fraction of the light is sent to a photodiode after the pinhole, allowing to track the power stability. Using a proportional-integral-derivative controller (PID), which regulates the AOM based on the photodiode's output signal, the laser power can be stabilized to a certain setpoint. The setpoint must be below the lower bound of

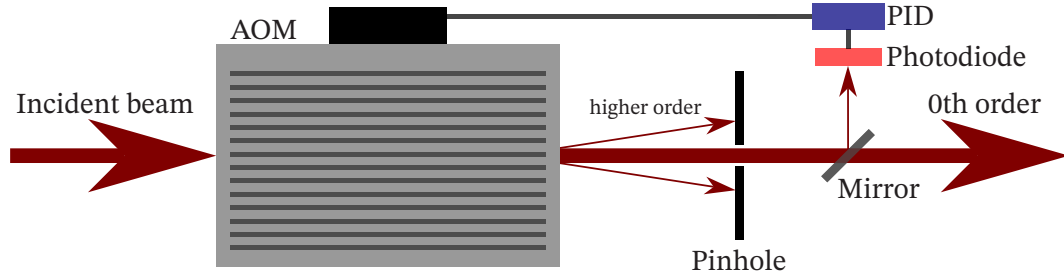


**Figure 3.2.1:** Illustration of the power stabilization setup.

the range in which the power is fluctuating, otherwise, the power cannot be stabilized properly.

Power stabilization is necessary in particular for the infrared laser beam, as the Rydberg laser is the one that is not stabilized to a specific transition frequency, but scanned. The frequency detuning leads to power fluctuations which are compensated by regulating the power via an AOM such that it is stabilized. The power stability provided by the AOMs is tracked. One may set a power range in which fluctuations are acceptable. If the power is out of range, the experimentalist is notified.

### 3.2.5 Frequency stabilization

Several kinds of fluctuations, like in temperature, current, air pressure and air moisture, lead to a slight change of the laser's emission frequency. The larger the emission frequency shifts away from the actual molecular transition frequency, the fewer NO particles can be excited on this transition. Especially the green transition is very narrow ( $\Delta\omega \approx 2\pi \cdot 70$  MHz at 1.1 mbar [20]), and thus a frequency shift of several MHz will lead to a vanishing Rydberg signal if the drifts are not counteracted. The time-scales of such frequency drifts are small and may be in the order of some minutes. Thus, long-term measurements of the Rydberg signal will not be possible, as the Rydberg signal's amplitude will decrease over time. Regarding the possible application of a breath-gas sensor, it is also more user-friendly, if there is a mechanism that counteracts the laser's drift and tunes it back to the transition frequency automatically. The frequency stabilized lasers are the UV and the green one. For the measurements performed, the Rydberg laser is scanned. Locking the Rydberg laser to a specific wavelength will be important in the future.

For the frequency stabilization or locking, a stabilization setup based on the Pound-Drever-Hall (PDH) technique is used. A brief introduction based on [47] is given here. A Fabry-Pérot interferometer is characterized by its free spectral range (FSR). The FSR reads

$$\text{FSR} = \frac{c}{2L}. \quad (3.3)$$

The length of the cavity is  $L$ . Light is only transmitted if its frequency is an integer multiple of the FSR. Thus, one gets a frequency spectrum of equally spaced transmission lines at intervals of the FSR. When the transmission is maximal, the reflected light is minimal. The reflected signal is the one relevant to the PDH method. Below the resonance, the derivative of the reflected intensity is negative, and above, it is positive. By slightly modulating the frequency of the laser and looking at the change of the reflected intensity one may conclude how the laser has to be tuned to be on a resonance again [47]. Based on that and by demodulating the laser's signal one can create an error signal. The error signal provides the information necessary for a PID to give feedback to counteract the frequency drifts.

The actual stabilization setup is built in such a way, that many different lasers can be stabilized. First of all, a so-called reference laser is frequency stabilized by locking it to a cavity peak of an ultra-low expansion cavity (ULE) and has been built and set up in the scope of [48]. As the name suggests, the reference laser serves as a reference for the Fabry-Pérot cavities, which are called transfer cavities. The estimated error due to small fluctuations is  $\Delta\omega_{\text{ref}} = 2\pi \cdot 121 \text{ kHz}$  [49]. Fractions of the reference laser's beam are directed to several transfer cavities. Each target laser has its own transfer cavity. Due to a piezo element, which can slightly tune the mirror on one side of the cavity, its length can be modulated. By doing so, one may stabilize the length of the transfer cavities to a cavity peak of the reference laser. Now, small beam fractions of the lasers to be locked on the molecular transition frequency are coupled into an electro-optical modulator (EOM) and then directed through the transfer cavities. The frequency of the molecular transition frequency is usually not an integer multiple of the cavity's FSR. The EOM modulates the phase of the laser beam leading to two sidebands at  $\omega_{\text{laser}} \pm \omega_{\text{EOM}}$ . Thus, the cavity peaks in the form of sidebands and consequently the error signal can be tuned, such that it is exactly at the position of the molecular transition frequency. Following that, the lasers can be locked to the specific transition frequency. It is important to adjust the values of the PIDs to obtain a stable lock. To keep track of the situation if the different stabilizations are working, the transfer cavity's transmission signals are recorded. If the transmission signal drops, the experimentalist is notified. The overall experimental procedure will be explained in a separate section. If the UV system and the green laser system are frequency stabilized and the Rydberg laser is the one detuned around the Rydberg transition, the estimated error of the frequency axis is  $2\pi \cdot 2.5 \text{ MHz}$  [20].

### 3.3 Gas mixing setup

The gas mixing unit allows the creation of a defined gas mixture of NO and N<sub>2</sub> by setting a specific gas flow using mass flow controllers and reach a stable pressure inside the measurement cell using valves. Pressure control is important. In order to lock the UV laser system on the molecular transition, the pressure inside the cell has to be set to around 1 mbar, otherwise the voltage signal gained by collisional ionization is too small for a precise locking compared to the recorded background noise. On the other hand, to measure a Rydberg signal, for e.g. a Stark map, the pressure should be one to two orders of magnitude smaller to reduce collisional broadening. There are pressure gauges installed at the inlet and outlet of the cell. By adjusting butterfly valves one may set these pressures to nearly the same value, to minimize the pressure gradient and allow one to state, that the actual pressure inside the cell is the average of these two pressure values. There are two external gas inlets available, an NO and an N<sub>2</sub> gas bottle can be separately connected to the setup. Gas mixtures of different gases like NO and N<sub>2</sub> in a specific proportion can be produced using mass flow controllers (MFC). The MFCs set the gas flow, thus enabling to control the pressure inside the cell in a precise and possibly automatic way. Experiments with gas mixtures of NO and N<sub>2</sub> are interesting from a physical point of view, as will be seen in the next chapter. However, N<sub>2</sub> is the main ingredient of human breath. Thus, pre-tests regarding the realization of a breath gas sensor can be done. The pressure and density of the gas inside the cell is given by the ideal gas law to a good approximation

$$p = Nk_B T . \quad (3.4)$$

The pressure is  $p$ , the gas density is  $N$ , the Boltzmann constant is  $k_B$  and the temperature inside the lab is about  $T = 293$  K. The gas mixing setup has been described in-depth in [50].

#### 3.3.1 Mass flow controllers

There are four MFCs and each of them has a different flow range which is given in standard cubic centimeters per minute (sccm). The MFCs with a maximum flow of 50 000 sccm and 2000 sccm were not in use in the scope of this work and their connection to the inlet gas line has been closed off by valves. However, the MFCs in use have the following properties:

**Table 3.3.1:** Flow properties of the two MFCs used

Maximum flow (sccm)	Minimum flow (sccm)
5	0.1
100	1.6

For a high gas mixture precision the overlap of the flow rates of both MFCs should be at least 20 % [50].

### 3.3.2 Pump system

The pump system contains a turbo pump and a diaphragm pump. If only the diaphragm is turned on, a pressure of about 8 mbar can be reached inside the cell. The additional turbo pump leads to a pressure in the range between  $10^{-5}$  mbar and  $10^{-4}$  mbar. Performing an experiment with NO gas mixtures, one may set stable pressures in the range between  $10^{-3}$  mbar and 1.5 mbar using the butterfly valves and the MFCs. By partially closing the butterfly valve in front of the cell, one may regulate the inlet flow of the cell. Using this valve one may set how much of the gas mixture is actually going into the cell and how much is going directly to the turbo pump. Another butterfly valve after the cell's outlet allows the control of the fraction of gas directed to a thin throttling line which reduces the flow to the pumps. Both valves are adjusted, such that the inlet and outlet gauges show similar values. Finally, a stable pressure inside the cell is achieved.

### 3.3.3 Experimental details

For measurements with pure NO, only the MFC with a maximum flow of 5 sccm is in use. The valve connecting the other MFC to the other gas inlet is closed to reduce background gas flow due to leakage. The 100 sccm MFC pipe is opened only if experiments including  $N_2$  are done. The pressure should stay below 1.5 mbar to not damage the turbo pump. If the butterfly valves are fully open, this threshold is approached at a gas flow above 90 sccm. To access higher pressures the procedure is the following: The valve at the outlet of the cell is closed. Then the cell is filled with the gas mixture to a certain pressure and the MFCs are closed. Now, the valve in front of the cell is also closed and a stable pressure inside the closed cell is reached. Thus, measurements can be run with pressures above 1.5 mbar. Afterwards, the inlet and outlet valves are re-opened, and the cell is evacuated.

### 3.4 Experimental measurement cell

The heart of the setup is the measurement cell including the electrodes and the PCB with a TIA. A picture is shown in 3.1.2. The main considerations when designing the cell were mainly a homogeneous electric field, low noise and fast feedback of the TIA. The design of the PCB is based on a cooperation with the Institute of Smart Sensors (IIS) at the University of Stuttgart.

The glass cell is made of borosilicate for technical reasons. Since borosilicate absorbs UV light, quartz windows are used, such that the UV beam may enter the cell. On the top of the cell, the PCB board is glued. It includes a TIA on the top, and on the PCB's bottom side an electrode pointing inside the cell is glued. The bottom side electrode is a copper plate. The homogeneity of the electric field is supposed to be provided by a big electrode area which is  $472 \text{ mm}^2$  and a small electrode distance of  $0.84 \text{ cm}$ . In order to reduce environmental noise detected by the TIA, the upper electrode is divided into an inner and an outer section by a guard ring. However, the potential is the same in both sections thus preventing leakage currents. Only the charges bumping into the inner area are detected by the electric circuit and the TIA. The inner area is just above the excitation volume, so the larger amount of charges is supposed to bump into the inner and not the outer section. Due to the fact that only the inner area is connected to the TIA, environmental noise collected through the big electrode is reduced. The voltage measured, according to Ohm's law is

$$U_{\text{out}} = R_{\text{TIA}} \cdot I. \quad (3.5)$$

The feedback resistance of the TIA is  $R_{\text{TIA}} = 1 \text{ G}\Omega$ . Thus, an output voltage of  $U_{\text{out}} = 1 \text{ V}$  would correspond to a detected current of  $I = 1 \text{ nA}$ . A more in-depth description of the electrical circuit is given in [20]. Additionally, we have to take the rise and fall time  $\tau_{\text{TIA}}$  of the TIA into account. A more detailed description is given in the next subsections.

#### 3.4.1 Electric field

The electric field  $F$  of a plate capacitor in the ideal case is given by

$$F = \frac{U}{d}. \quad (3.6)$$

Here,  $U$  is the offset voltage applied between the electrodes, and  $d$  is the electrode distance. An analysis of the actual electric field inside the cell has been done in the scope of a Bachelor's thesis [51]. Despite non-linearities of the electric field inside the cell due to surface and space charges, equation 3.6 holds to a good agreement. This is supported by the fact, that it was possible to align theoretically calculated Stark maps to measured ones, see section 4.2. For the Stark maps measured, as well as for all other measurements, an electric field according to (3.6) has been supposed.

### 3.4.2 Electronic limits due to the TIA

There are some experimental parameters, which are directly linked to the aforementioned rise and fall time  $\tau$  of the TIA. It is crucial to know the electronic limits, otherwise the experimental results may be falsified.

The TIA can be described as a passive low-pass filter in first order. In this case the output voltage, if there is an instantaneous current signal input to the TIA is [52, 53]

$$V(t) = A \cdot \left( 1 - \exp\left(-\frac{t - t_0}{\tau_{\text{rise}}}\right) \right) + \text{offset}, \quad (3.7)$$

including the rise time  $\tau_{\text{rise}}$  and the amplitude  $A$ . Here,  $t_0 \leq t \leq t_1$  holds. The signal's drop is described by

$$V(t) = A \cdot \left( \exp\left(-\frac{t - t_1}{\tau_{\text{fall}}}\right) \right) + \text{offset}, \quad (3.8)$$

including the fall time  $\tau_{\text{fall}}$  and  $t > t_1$ .  $\tau_{\text{rise}}$  is the time it takes that the TIA's output signal has increased from 10% to 90% of  $A$ .  $\tau_{\text{fall}}$  describes the time vice versa. To determine the average of the rise and fall time, the UV and green laser system has been locked to the transition. Via the AOM the green laserbeam's power is periodically highly reduced and the TIA's output voltage is measured. An average value of  $\tau = 121 \mu\text{s}$  has been extracted from fits (equation 3.7 and 3.8) to the output signal [52].

In the scope of a Bachelor's thesis [52] the investigation and optimization of parameters has been done based upon the usage of a lock-in amplifier. The lock-in amplifier has been introduced to improve the signal-to-noise ratio (SNR). The working principle of a lock-in amplifier is based on a periodic modulation of the measurement signal, multiplied by a reference signal of the same frequency. Afterwards, the signal passes a low-pass filter, finally leading to a DC output signal. The SNR is a characteristic quantity to describe the quality of the signal. The modulation, i.e. chopping of the green or infrared laser beams, is done via the AOMs. Despite the fact, that the modulation of the infrared laser beam leads to a marginally better SNR, the green laser beam is the one chosen for the power modulation procedure in the experiment. The Rydberg laser is the one scanned during the measurements. Power fluctuations of up to 50% are observed without power stabilization through the AOM. Proper power stabilization and modulation at once is more challenging and at this point not needed. Modulating the Rydberg laser beam might be a good option if the Rydberg laser is locked to a specific transition frequency.

The state of choice for the investigation of the experimental parameters was 22(4), specifically the central line of the high- $l$  manifold, which has been fitted, and the width extracted [52]. The first important parameter based on  $\tau$  is the scan velocity of the laser. This parameter has to be chosen properly based on the TIA's time constant  $\tau$ , regardless of whether the lock-in is used or not, as this may alter the lineshape if the scan velocity is too high. In this paragraph, the results including a lock-in are presented. Scan velocities between  $0.1 \text{ GHz s}^{-1}$  and  $1.6 \text{ GHz s}^{-1}$  did not lead to significant line broadening. The

first crucial parameter of the lock-in is the time constant. Time constants up to 10 ms at a scan velocity of  $\approx 0.7 \text{ GHz s}^{-1}$  do not lead to a line broadening of the measured peak. Despite a marginal broadening, 30 ms is the time constant of choice, due to the best SNR. Here, the reference frequency chosen is 475 Hz. An upper bound can be estimated to be 826 Hz, however, a bigger chopping frequency leads to a loss in the signal's amplitude. The lock-in's low pass filter slope is set to  $18 \text{ dB oct}^{-1}$ . The sensitivity, which is basically an amplification factor of the lock-in's output signal, has to be adjusted during the measurements depending on the signal's amplitude to prevent reaching the lock-in amplifier's output limit leading to a saturation of the output signal. Based on these results, the lock-in has been used for the final experimental measurements.

## 3.5 Experimental procedure

This section summarizes the steps to perform NO Rydberg signal measurements, based on the aforementioned introduction to the whole experimental setup. Therefore, first of all, an insight is given on how the knowledge of the transition wavelengths is extracted. Based on the chosen transitions the UV and green laser are locked and the measurement is set up. The procedure is described in a subsection. Finally, an insight is given on the measurement data evaluation.

### 3.5.1 Calculation of the transition wavelengths

As a recap, our Rydberg excitation path reads

$$n(N^+) \leftarrow \text{H}^2\Sigma^+ \leftarrow \text{A}^2\Sigma^+ \leftarrow \text{X}^2\Pi_{3/2}. \quad (3.9)$$

The calculation of the wavelength of the first transition  $\text{A}^2\Sigma^+ \leftarrow \text{X}^2\Pi_{3/2}$  for different rotational branches has at first been done via PGOPHER [28] using constants from [54] and then adjusted during the locking procedure. Information considering the wavelengths of the branches on the intermediate transition  $\text{H}^2\Sigma^+ \leftarrow \text{A}^2\Sigma^+$  can be extracted from the paper of Ogi [31]. In order to get the wavelengths of the Rydberg states  $n(N^+)$  some calculations have to be performed. Based on the deduced equation (2.16) for the rovibrational spectrum, the energy of the NO Rydberg states can be calculated. The vibrational terms in equation (2.16) can be neglected as  $v = 0$  dominates. The electronic contribution is calculated based on the Rydberg formula (2.18). The final equation reads [23]

$$\frac{E(n, N^+)}{hc} = W^+ + B_{\text{NO}}^+ N^+ N^+ (N^+ + 1) - D_{\text{NO}}^+ (N^+ (N^+ + 1))^2 - hc \frac{R_{\text{NO}}}{n^2}. \quad (3.10)$$

The effective principal quantum number has been set to  $n$  as the quantum defects are not relevant for this determination. Here, the specific molecular constants of NO have to be inserted in units of the wavenumber.  $W^+$  is the absolute ionization threshold which depends on the branches chosen for the lower transitions. It has been experimentally investigated in [20].  $B_{\text{NO}}^+$  is the rotational constant,  $D_{\text{NO}}^+$  the centrifugal distortion constant and  $R_{\text{NO}}$  is the Rydberg constant of NO. Based on equation (3.10) the wavelengths of different Rydberg states  $n(N^+)$  can be calculated. The full derivation of the calculation is given in [20]. A summary of the wavelengths of the different rotational branches the lasers have been locked to is given in the following tables 3.5.1 and 3.5.2. The wavemeter's readout error is included. However, the actual readout of the wavemeter is the wavelength of the laser's output and not the one after the frequency quadrupling (UV system) or doubling (green system).

**Table 3.5.1:** The table shows the transition wavelengths of different branches of the UV transition the lasers have been locked to in order to access different  $N^+$  series, gained from the wavemeter's readout after locking to the molecular transition including the wavemeter's uncertainty.

Excitable $N^+$	$A^2\Sigma^+ \leftarrow X^2\Pi_{3/2}$	wavelength (nm)
0 & 2	$P_{12}(2.5)$	226.9145(4)
1 & 3	$P_{12}(3.5)$	226.9356(4)
2 & 4	$P_{12}(4.5)$	226.9538(4)
3 & 5	$P_{12}(5.5)$	226.9695(4)
4 & 6	$P_{12}(6.5)$	226.9823(4)

**Table 3.5.2:** The table shows the transition wavelengths of the second transition.

Excitable $N^+$	$H^2\Sigma^+ \leftarrow A^2\Sigma^+$	wavelength (nm)
0 & 2	$R_{11}(1.5)$	540.3580(12)
1 & 3	$R_{11}(2.5)$	540.3889(12)
2 & 4	$R_{11}(3.5)$	540.4232(12)
3 & 5	$R_{11}(4.5)$	540.4584(12)
4 & 6	$R_{11}(5.5)$	540.4936(12)

### 3.5.2 Setting up the measurement

Setting up a measurement requires different steps, which are basically the same for all kinds of measurements of the Rydberg signal. The procedure of locking the lasers has been discussed in section 3.2.5 and can be broken down into five main steps until a Rydberg signal is gained and a measurement run can be started.

1. Stabilization of the reference laser's frequency.
  - A stable reference lock is essential, otherwise, all other locks are likely to drop. The optimal parameters are based on [49].
2. Stabilization of the transfer cavities' length.
  - There are in total 3 transfer cavities to be stabilized, one for each laser system.
  - Even though the Rydberg laser's output frequency is not stabilized, its transfer cavity's length is locked as the transmission peaks of the Rydberg laser passing through the cavity are used to derive a frequency axis.
3. Lock the UV laser system on the molecular transition frequency.
  - The pressure inside the cell is set to  $\approx 1$  mbar, as well as a high electric field of at least 10 V/cm in order to gain a good visible measurement signal on the oscilloscope in terms of SNR.

- The UV laser's frequency is periodically detuned around the transition frequency of the branch chosen and using the EOM a sideband peak is shifted to the position of the molecular transition.
  - Using a PID and the stabilized transfer cavity the UV laser system's frequency is locked.
4. Lock the green laser system on the molecular transition frequency
    - Same procedure as for the UV laser frequency stabilization.
    - One may switch to the lock-in amplifier and chop the green transition or continue using the TIA's output to gain the measurement signal on the oscilloscope.
    - Due to the narrow linewidth the sideband has to be shifted very precisely.
    - After frequency stabilization, the laser power is stabilized via an AOM.
  5. Tune the Rydberg laser to the Rydberg state chosen.
    - The pressure inside the cell is reduced to several tens of  $\mu\text{bar}$ . The electric field is set to about 1 V/cm to avoid splittings due to the Stark effect when searching for the signal and setting the scan range.
    - The Rydberg laser is scanned continuously in a sawtooth function-like manner, around the transition frequency. The Rydberg laser's scan range and velocity are set.
    - Power stabilization is done via the AOM.

Now, a measurement run can be started. Different measurement scripts, which have been written in Python, are used to automatize the measurement run in large parts. The script may control parameters like the offset voltage of the electrodes and the flow of different MFCs. During a measurement run, one of these parameters is changed by the script by a specific step size and up to a certain limit. Furthermore, the script reads out and saves the data recorded by the oscilloscope, as well as parameters of the lock-in amplifier, the values of the pressure gauges, and the wavelengths of the lasers on the wavemeter.

The data recorded by the oscilloscope is the measurement signal, which is either the direct output of the TIA or if the lock-in is used, the lock-in amplifier's output. In this case, the lock-in amplifier's parameters are readout and recorded by the script too. These are the phase, the sensitivity, the integration time, the low-pass filter slope, and the reference frequency. The sensitivity is important for the back-calculation of the TIA's output. Besides the measurement signal, the transmission peaks of the Rydberg laser for the frequency axis generation, and the laser's trigger is recorded by the oscilloscope. Recording the laser's trigger signal is not necessary, but is done to review if the whole Rydberg laser scan has been properly depicted on the oscilloscope. The script works in that way that the experimental parameter investigated is set, and then a single trace including the aforementioned parameters is recorded. Afterwards, the experimental parameter is changed and a single trace is recorded again until the upper limit of the parameter is reached or a lock drops. In this case the script stops. Here, the measurement

data of one single Rydberg laser scan over the whole scan range set in the Rydberg laser's interface is referred to as a single trace.

Of course, one may also record individual single traces for test purposes, and the whole frequency stabilization is only necessary for long-term measurement runs. In this case, the UV and green laser system have to be re-adjusted regularly by hand to the wavelengths given in the tables 3.5.1 and 3.5.2 to counteract the decrease of the Rydberg signal over time.

#### 3.5.3 Data evaluation

The data measured by the oscilloscope is the time and the voltage. Despite the fact, that one may set a constant scan range and scan time of the Rydberg laser, one may not assume that the Rydberg frequency detuning is linear and thus the time to frequency conversion is therefore not linear as well. In order to gain a frequency axis, the transmission cavity peaks of the Rydberg laser's signal recorded are used. Since the transfer cavity's length is stabilized and its FSR is known, the transmission peaks recorded by the oscilloscope during one Rydberg laser scan can be used for the evaluation procedure. The evaluation has been implemented in a Python script, and described in more detail in [20]. The script's function is based on finding the positions of the cavity peaks on the time axis and fitting the found positions using a polynomial function of the third order. The algorithm is optimized in such a way, that slight changes in the laser's scan as well as small fluctuations in the length of the transfer cavity are considered in the frequency axis generation if several single traces with different pressures or electric fields are recorded in a long-term run. This means that the cavity peaks are tracked and aligned. Finally, the frequency axis is based on the Rydberg scan range which contains all the same cavity peaks in the time domain of all single traces. Thus, the actual frequency range shrinks due to cutting the upper and lower bound regions of the laser's scan. Note, that the frequency axis is not absolute, but describes the frequency detuning of the Rydberg laser. The current detected is calculated via Ohm's law (3.5). If the lock-in is in use, the sensitivity gives information on the additional conversion factor to the actual TIA signal. The electric field is calculated based on the formula of an ideal plate capacitor (3.4.1) and the gas density may be calculated via the ideal gas law (3.4). Finally, the Rydberg signal is smoothed by a Savitzky-Golay filter in an appropriate way, such that the lineshape is not negatively affected and thus, further evaluation steps which will be described in the appropriate chapters can be done with less computational capacity.

## 4 Experimental results

This chapter gives an overview on the main results gained in the scope of this work. Details on the common experimental realization were given in the last chapter. The results can be broken down into two main topics, namely the investigation of collisional shifts and broadening of Rydberg states of NO, as well as the investigation of the Stark effect. Both investigations are interesting in terms of the realization of a trace gas sensor, as well as from a physical point of view.

### 4.1 Collisional shift and broadening

The results explained in this section have already been published in [55] and discussed elaborately in [20]. Regarding the realization of a trace-gas sensor of NO a high selectivity is necessary. This is ensured by the three-photon excitation scheme using cw laser systems. On the other hand, different broadening mechanisms as introduced in subsection 2.4.2 may contribute to a broadening of the spectroscopic line. Gas density dependent measurements allow us to determine a region, where the collisional broadening contribution is sufficiently small, ensuring a high selectivity and excitation efficiency. Furthermore, due to elastic collisions, the Rydberg line may experience a density dependent shift. This is an effect one has to pay attention to if the trace gas sensor is operating at different pressures while the Rydberg transition is locked. The latter one will be done in the future. The gas mixing setup allows to set different pressures inside the measurement cell, and mix NO and N<sub>2</sub> in different concentrations making this kind of investigation possible. The results can be explained based on the Fermi shift [7] and compared with similar investigations from other groups [8, 9].

#### 4.1.1 Pressure dependent measurement procedure

The parameters and measurement procedure used for the investigation are based on good experience and previous investigations. The general experimental procedure has already been explained in the previous chapter in subsection 3.5.2. For the pressure dependent investigations, the lasers have been locked to the P<sub>12</sub>(6.5) branch for the UV transition and the R<sub>11</sub>(5.5) branch for the green transition, thus allowing to excite Rydberg states  $n(N^+)$  in the  $N^+ = 4$  and  $N^+ = 6$  rotational series. The green transition is modulated to improve the SNR. The lock-in amplifier's parameters have been explained

in section 3.4. The lock-in amplifier's time constant is set to 30 ms, while the scan velocity of the Rydberg laser is set in the interface to 13 GHz in 19.9 s. These parameters have no significant impact on the lineshape in terms of broadening. Different states  $n(N^+)$  have been chosen for the investigation. The Rydberg line of interest is the central line of the high- $l$  manifold which is not much shifting when applying different electric fields. The voltage between the electrodes of the cell is set to  $-10$  V, leading to an electric field of approximately  $-11.9$  V cm $^{-1}$ , causing a Stark splitting that allows to separate the central line. The Rydberg laser is periodically detuned around the central line of the high- $l$  manifold of the Rydberg state chosen.

In the case of pressure-dependent measurements with pure NO, only the MFC with a maximum flow of 5 sccm is used. In the beginning, the flow is set to about 1 sccm, and the butterfly valves are adjusted such that the inlet and outlet pressure gauges show similar values. The pressure at the beginning of the measurement run is set to a value roughly at 10  $\mu$ bar. Here, a sufficiently good signal in terms of SNR is gained, in order to do the Rydberg line fitting routine which is described later.

In the case of measurements with NO and N $_2$  the 100 sccm MFC is used to set the flow of N $_2$ . In the beginning, the flow of NO is set to 0.2 sccm and for the other MFC controlling the flow of N $_2$ , the latter one is set to 1.6 sccm. The valves are adjusted such that a total pressure of roughly 0.2 mbar inside the cell is reached and a good visible Rydberg signal is observed.

The measurement run is performed in an automatic way using a Python script as described in subsection 3.5.2. The gas density inside the cell is increased by increasing the MFC's flow. The step size chosen depends on the alignment of the valves. In the case of measurements with pure NO, if the MFC's maximum flow is approached, the measurement run is stopped. The MFC's flow is set to a lower value now, and the valves are adjusted such that higher pressure ranges can be reached. In the case of measurements including N $_2$  the flow of NO is kept constant, and only the flow of N $_2$  is increased. The flow values of the MFCs are important to readout in this case, in order to be able to translate the total pressure to partial pressures of NO and N $_2$ . After the script sets a specific flow of the MFC, the oscilloscope is set to wait 45 s to ensure a stable pressure inside the cell before acquiring the channels. Afterwards, the signals and experimental parameters as described in subsection 3.5.2 are saved automatically. The whole measurement run consists of several single traces with different gas densities.

During the measurement run, the lock-in amplifier's sensitivity is constantly adjusted. If a pressure of over 1.5 mbar is reached, the script interrupts the measurement and sets the MFC's flow to zero. If the lock of the Rydberg laser's transfer cavity is lost, the whole measurement run has to be repeated. The whole measurement run takes up to two hours.

Besides the aforementioned investigation of the Rydberg line, the green transition has also been investigated in terms of pressure dependency for pure NO. Here, only the UV laser system has been locked, and the green transition has been the one scanned.

For the pressure dependent measurements, the mean intensity of the UV laser beam has been about  $1.8 \text{ mW/mm}^2$ . The intensity of the green laser beam has been about  $480 \text{ mW/mm}^2$ , and the intensity of the infrared laser beam has been in a range from  $47 \text{ mW/mm}^2$  to  $66 \text{ mW/mm}^2$ .

#### 4.1.2 Evaluation

The overall evaluation routine to gain the current detected and the frequency axis in terms of the detuning of the Rydberg laser has already been explained in subsection 3.5.3. Exemplary, a single trace of a measurement run is shown in figure 4.1.1. Here, the high- $l$  manifold of the state 22(6) is visible. The plot shows the current detected depending on the Rydberg laser detuning at a pressure of  $150.5 \mu\text{bar}$ . Note, that the frequency is the ordinary frequency  $f$  and not the angular frequency  $\omega$ , which are related by  $\omega = 2\pi f$ . The central line, which also has the highest peak value, is well visible and marked in the plot.

For the purpose of extracting the peak position and the width in terms of FWHM of the central line, a fitting routine has been established. The function used to fit the measurement data of the central line is the Voigt function  $f_V(\Delta f)$  as defined in equation (2.24) and a polynomial function  $P_2(\Delta f)$  of second order accounting for the baseline

$$f_{\text{fit}}(\Delta f) = f_V(\Delta f) + P_2(\Delta f). \quad (4.1)$$

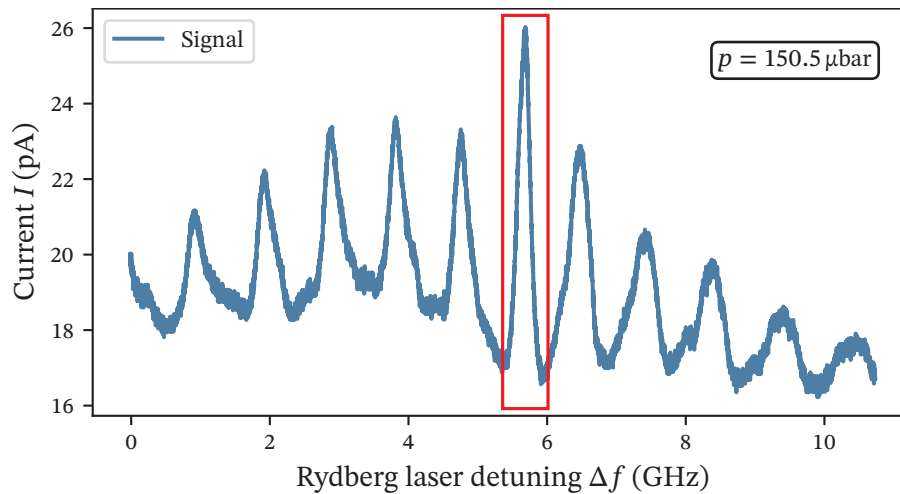


**Figure 4.1.1:** An evaluated single trace of the pressure measurement run of the state 22(6) with pure NO showing the current detected depending on the Rydberg laser detuning. The central line is marked with a red box.

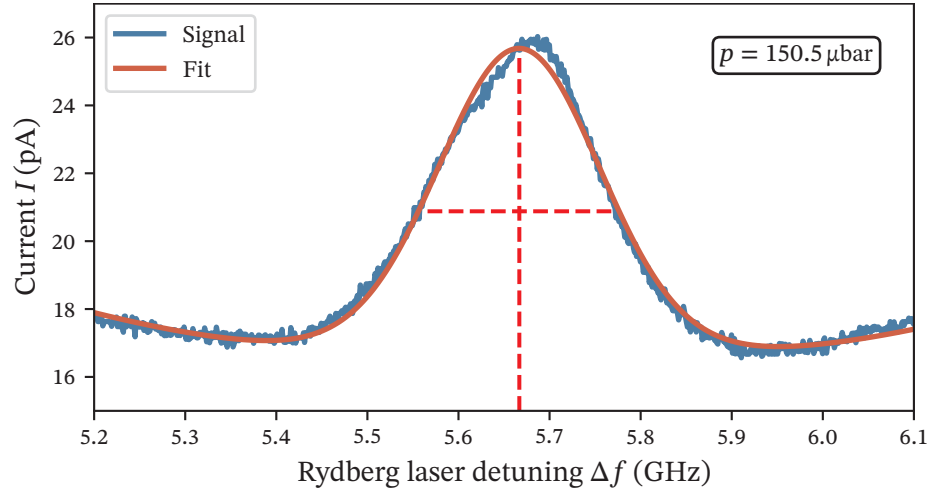


**Figure 4.1.2:** Zoom-in to the central line of the single trace shown in the figure 4.1.1. A Voigt function including a polynomial function of second order to account for the baseline is used to fit the measured Rydberg signal.

Although collisional broadening is supposed to be homogeneous, the Voigt function leads to the best fit results. An example of a fit based on equation (4.1) is shown in figure 4.1.2. Here, a zoom-in to the central line of the single trace in the figure 4.1.1 is shown. Note, that the neighboring peaks are fitted as well for checking purposes, but no further evaluation is done for the side peaks. All single traces of the measurement run are evaluated in this way, and the FWHM and the peak positions of the central line are extracted. The boundaries and initial peak positions are set manually for a single trace. Based on that, the fitting routine for all traces is done automatically.

The FWHM of the central lines of all single traces of the state 22(6) depending on the density of NO is depicted in figure 4.1.3. The pressure to density conversion is done via the ideal gas law as described in equation (3.4). Note, that in the case of measurements with both NO and N<sub>2</sub>, the partial pressure of N<sub>2</sub> is calculated based on the total pressure recorded and the flows of both MFCs. Now, the data points of the FWHM at different background gas densities are fitted. In the exemplary case shown before the background gas is NO itself. According to equation (2.33), a linear behavior of the collisional broadening is expected. However, there are additional contributions to the linewidth, see subsection 2.4.2. Concrete values of the different contributions are not known. An offset taking care of the residual broadening is included in the fit function

$$f_{\text{fit,FWHM}}(N) = \sqrt{\text{off}^2 + \left(\frac{\text{FWHM}}{N} \cdot N\right)^2}. \quad (4.2)$$

The linear behavior of the collisional broadening is encoded in the broadening rate  $\text{FWHM} \cdot N^{-1}$  which is the fit parameter of interest. The fit to the FWHM of the state

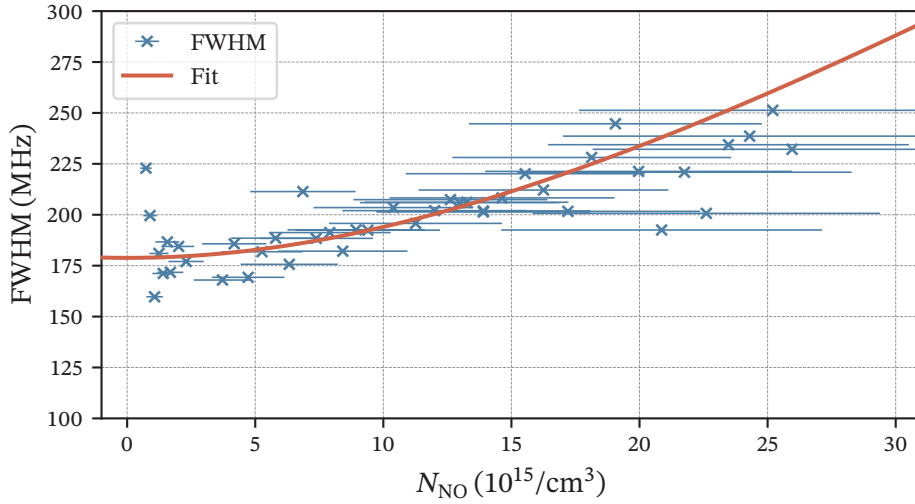


**Figure 4.1.3:** The FWHM extracted from the measurement and fitting run of the state 22(6) with pure NO. The error bars show the uncertainty arising from the pressure gauges.

22(6) is also shown in figure 4.1.3.

For the shifts of the peak of the central line the evaluation is similar. The frequency shift  $\delta$  of the central line's peak is relative to the mean peak position of the traces taken at the lowest pressures. Here, the fit function is based on the Fermi shift (equation (2.45)), which also scales linearly with the background gas density leading to the fit function

$$f_{\text{fit},\delta}(N) = \frac{\delta}{N} \cdot N. \quad (4.3)$$

Here, the fit parameter of interest is the shift rate  $\delta \cdot N^{-1}$ .

As already mentioned, an additional measurement has been done where the UV laser system has been locked and the green one has been the one periodically detuned around the transition. Here, the fit function for the FWHM of the  $\text{H}^2\Sigma^+$ -state is

$$f_{\text{fit,FWHM,green}}(N) = \frac{\text{FWHM}_{\text{green}}}{N} \cdot N + \text{off}, \quad (4.4)$$

and for the shift

$$f_{\text{fit},\delta,\text{green}}(N) = \frac{\delta_{\text{green}}}{N} \cdot N \quad (4.5)$$

holds. To determine the broadening and shift rate, if the Rydberg laser is turned on, the wavevector mismatch based on [56] has to be considered. The different signs occur because the UV beam ( $k_1$ ) is counterpropagating towards the green ( $k_2$ ) and infrared one ( $k_3$ ). The wavevector mismatch reads

$$k = \frac{k_1 - k_2 - k_3}{k_1 - k_2} = \frac{1/\lambda_1 - 1/\lambda_2 - 1/\lambda_3}{1/\lambda_1 - 1/\lambda_2} \approx 0.53, \quad (4.6)$$

with  $\lambda_1 = 226$  nm,  $\lambda_2 = 540$  nm and  $\lambda_3 = 835$  nm being the design wavelengths of the laser systems. For the measurements of the Rydberg signal the broadening and shift rate of the green transition determined by equation (4.4) and (4.5) have to be scaled with factor  $k$ .

### 4.1.3 Results

The results gained from the pressure dependent measurements are visible in the figure 4.1.4. The broadening rate  $\text{FWHM} \cdot N^{-1}$  and the shift rate  $\delta \cdot N^{-1}$  extracted through fits as given in equation (4.2) and (4.3) are summarized in table 4.1.1 including the error arising from the pressure gauges. The absolute pressure uncertainty of the gauges used is 30 %. The uncertainty of the frequency axis has been estimated to  $2\pi \cdot 2.5$  MHz [20] and is therefore not significant.

At first, we look at the broadening in terms of the FWHM of different Rydberg states. The broadening behavior of NO perturbed by itself compared to NO perturbed by  $\text{N}_2$  is similar and a linear density dependency is evident indicating a collisional broadening. However, the broadening rate in the case of NO perturbed by itself is slightly bigger. As already explained in section 2.3, the internal electronic structure of the ground state of NO and  $\text{N}_2$  differ only by the occupation of the  $\pi_{2p}^*$  orbital in the case of NO. The Rydberg electron and perturber cross section might be slightly bigger in the case of perturbation with pure NO, leading to a higher broadening rate. The broadening contribution due to the population of rotational levels from  $J = 0.5$  to  $J = 19.5$  in NO, which appears since a molecule has additional degrees of freedom compared to an atom, has been estimated to be significant for the broadening [20].

The behavior of the green transition is indicated by a green line in figure 4.1.4. The broadening and shift rate extracted from the fits (equation 4.4 and 4.5) are

$$\frac{\text{FWHM}_{\text{green}}}{N} = 0.637 \cdot 10^{-15} \text{ MHz cm}^3, \quad (4.7)$$

and the shift rate is

$$\frac{\delta_{\text{green}}}{N} = -0.258 \cdot 10^{-15} \text{ MHz cm}^3. \quad (4.8)$$

Scaled with the pre-factor  $k$  due to the wavevector mismatch leads to a broadening rate of

$$\frac{\text{FWHM}_{\text{green, scaled}}}{N} = 0.338 \cdot 10^{-15} \text{ MHz cm}^3, \quad (4.9)$$

and a shift rate of

$$\frac{\delta_{\text{green, scaled}}}{N} = -0.137 \cdot 10^{-15} \text{ MHz cm}^3 \quad (4.10)$$

for the Rydberg measurements. The shift and broadening rate is small compared to the shift rates observed for the Rydberg states as given in table 4.1.1. The appearance of a density-dependent shift of the green transition may give an additional indication of the necessity of the Voigt profile as the fit function of choice for the Rydberg line, on top of the molecule's degrees of freedom.

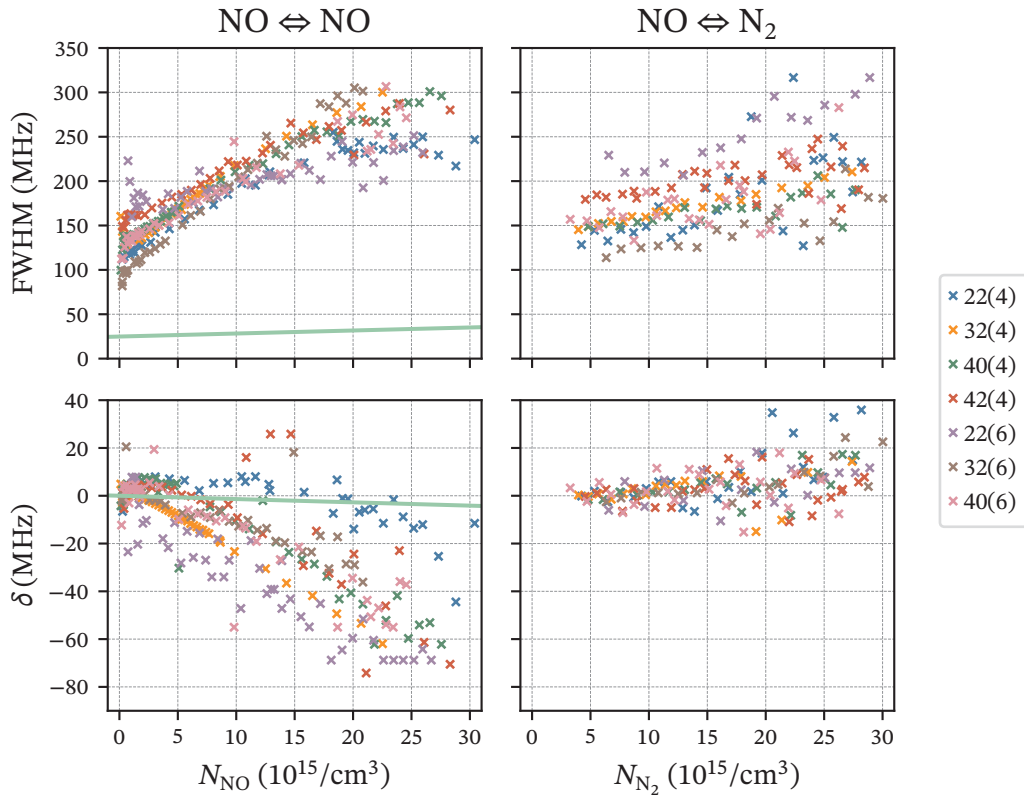


**Figure 4.1.4:** The linewidth of the central line in terms of the FWHM and the relative peak shift  $\delta$  extracted in the scope of the evaluation routine for several Rydberg states  $n(N^+)$ . The  $x$ -axis denotes the background gas density  $N$ , which is either NO itself or N<sub>2</sub>. Choosing the density instead of the pressure for the  $x$ -axis allows better comparison with results available in the literature. The density is proportional to the pressure, e.g. a density of  $30 \cdot 10^{15}/\text{cm}^3$  corresponds to a pressure of 1.2 mbar. In the case of measurements with N<sub>2</sub>, the density of NO is constant at approximately  $N_{\text{NO}} \approx 5 \cdot 10^{14}/\text{cm}^3$ , which corresponds to 20  $\mu\text{bar}$ . On the left hand side the results of measurements with pure NO are shown, while on the right hand side N<sub>2</sub> serves as a background gas. The green line shows the behavior of the peak width and shift of the green transition resulting from the fit functions given in the equations (4.4) and (4.5) and scaled considering the wavevector mismatch.

In the case of pure NO, the Rydberg line shifts to lower frequencies, i.e. a red shift can be seen. In the case of N<sub>2</sub> as a perturber, a small blue shift of the line is occurring. Shifts of Rydberg lines only occur in the case of elastic scattering. Since the shift appears to be linear, it can be attributed to elastic Rydberg electron and perturber scattering. A derivation of the Fermi shift has been given in subsection 2.4.3. The direction of the shift is an indicator of the dominating kind of interaction. In the case of pure NO, the scattering length might be negative, leading to a dominantly attractive interaction of the Rydberg electron and perturber, in the case of N<sub>2</sub> as perturber, it is the contrary case. As one can see elastic collisions are more dominating in the case of pure NO, due to the higher shift rate compared to the case where the perturber is N<sub>2</sub>. Due to several degrees of freedom and available states in the rovibrational spectrum of NO and N<sub>2</sub> allowing resonant inner energy exchange between the collisional partners, elastic scattering may be not expected in the first place. However, elastic collisions are occurring. The elastic kind of collisions between the NO molecules may arise due to an electron transfer and the formation of NO<sup>-</sup> leaving the overall inner energy of the molecule unchanged. Existence of NO<sup>-</sup> has been shown in [57].

It is interesting to note, that the state 22(4) behaves slightly different compared to the other Rydberg states. Here, in the case of pure NO, the shift rate is small compared to the other states investigated, and the shift rate in case of perturbation with N<sub>2</sub> is the highest (see table 4.1.1). One can also see in figure 4.1.4, that the shift of the central line of the state 22(4) may have higher order contributions, besides a linear one. This may indicate that apart from Rydberg electron and perturber scattering, a significant contribution due to Rydberg ion and perturber interaction may arise. The derivation of the linear behaving Fermi shift is based on the assumption of a significant amount of perturbers interacting with the Rydberg electron thus justifying the introduction of the average wavefunction in the scope of the derivation, see subsection 2.4.3. This might be not given in this case.

**Table 4.1.1:** Broadening and shift rates of the central line of measurements of different Rydberg states gained in the scope of the evaluation. The unit of the rates is 10<sup>-15</sup> MHz cm<sup>3</sup>. The error arising from the pressure gauges is given as well.

$n(N^+)$	NO $\Leftrightarrow$ NO		NO $\Leftrightarrow$ N <sub>2</sub>	
	FWHM · N <sup>-1</sup>	$\delta$ · N <sup>-1</sup>	FWHM · N <sup>-1</sup>	$\delta$ · N <sup>-1</sup>
22(4)	8.3(25)	-0.74(22)	7.4(22)	1.3(4)
32(4)	13.0(39)	-2.8(8)	5.5(16)	0.25(8)
40(4)	10.6(32)	-2.5(7)	4.0(12)	0.57(17)
42(4)	9.1(27)	-2.1(6)	4.0(12)	0.19(6)
22(6)	7.5(23)	-2.7(8)	9.2(28)	0.52(16)
32(6)	14.8(44)	-1.4(4)	4.9(15)	0.82(25)
40(6)	10.3(31)	-2.3(7)	6.1(18)	0.089(27)

**Table 4.1.2:** Broadening and shift rates of measurements of different Rydberg states in alkalis. In case of Füchtbauer et al. [8], potassium (K) perturbed by argon (Ar) has been investigated. Weber et al. [9] investigated rubidium (Rb) perturbed by argon. The unit of the rates is  $10^{-15}$  MHz cm<sup>3</sup>.

$n$	<b>K <math>\leftrightarrow</math> Ar</b>	<b>(<math>n</math>S) Rb <math>\leftrightarrow</math> Ar</b>	
	$\delta \cdot N^{-1}$	$\delta \cdot N^{-1}$	FWHM $\cdot N^{-1}$
21	-10.97	-4.76	1.46
23	-10.94	-4.94	1.56
25	-11.34	-5.02	1.66
27		-5	1.77
29		-5	1.8
33		-5.16	1.36
35		-5.04	1.36

The extraction of broadening and shift rates for different Rydberg states allows to compare these values to the investigations from Füchtbauer et al. [8] and Weber et al. [9]. In contrast to our investigation involving molecules, rare gas atoms served as perturbers in both groups' publications. The atoms excited to Rydberg states are alkalis. In the case of Füchtbauer et al., amongst other things, they investigated potassium, which has been perturbed by argon. Weber et al. investigated high  $n$ S states in rubidium perturbed by argon. The broadening and shift rates of these investigations are listed in table 4.1.2. In both cases, a red shift has been observed. The broadening rates in our case are up to one order of magnitude higher than the broadening rate in the publication of Weber et al. The shift rates extracted from our measurements with pure NO are in the same order of magnitude of both group's results, but multiple times smaller. Here, our shifts are roughly two times smaller compared to Weber et al., and about four times smaller compared to Füchtbauer et al. An explanation for the elastic scattering observed described in the aforementioned publications is more intuitive, as the rare gas atoms serving as perturber have fully occupied shells and resonant inner energy exchange due to the lack of rotational and vibrational degrees of freedom is unlikely. The latter fact might explain the higher shift rates observed in the other publications compared to our investigations. The higher broadening rates observed in measurements with NO are also attributed to the molecule's complexity compared to an atom.

#### 4.1.4 Conclusion

The investigation of the collisional broadening of Rydberg lines of NO provided the knowledge, that in order to gain a high selectivity of the trace gas sensor an operation at low pressures, i.e. in the low  $\mu$ bar regime is desirable due to comparably high broadening rates. If the concentration of NO is extremely small as it is in breath gas, such low pressures will not be suitable for a good Rydberg signal detection in terms of SNR in

the current setup. An improvement of the sensitivity of the measurement cell will have to be done to account for that. However, in the case of measurements with pure NO, operation around  $70 \mu\text{bar}$  provides a sweetspot between sufficiently good SNR and low collisional broadening, which will be important in the next chapter.

From a physical point of view, the linear behaving Fermi shift could be observed and compared to other publications. These results, published in [55] might be a stimulation to a more in-depth theoretical investigation of the actual processes occurring. The fact, that we are dealing with Rydberg states in a molecule, namely NO interacting with other molecules and not atoms makes the theoretical investigation more complicated. Here, a determination of scattering lengths is desirable. Moreover, quantitative estimates regarding the contributions of the forces interacting might be extracted from the collisional shift and broadening [58].

## 4.2 Stark effect

Following the results of the previous chapter providing the information about collisional broadening effects, the Stark effect in NO is investigated. The voltage between the electrodes i.e. the electric field inside the measurement cell can be varied stepwise making this kind of measurements possible. Stark map measurements may give the information, which Rydberg states are possible candidates for a sensor application. The criterion is that the state is unaffected by the Stark shift and is thus not sensitive to fluctuations of a static electric field that may occur in the sensor to-be. Otherwise, the Rydberg transition frequency will have to be adjusted and no constant lock of the Rydberg laser is possible. Moreover, an estimation may be given in which range the electric field has to be to gain the highest Rydberg signals.

However, the main focus of the investigations has been on the measurement of several highly-resolved Stark maps of different Rydberg states thus providing data for theoretical investigations and the determination of quantum defects. The measurement procedure has been optimized to improve the quality of the Stark Maps. The theoretical investigations of the Stark map measurements are done by Prof. Stephen Hogan and Dr. Matthew Rayment from the University College London.

The Rydberg state of main interest is  $22(0)$ . Since  $N^+ = 0$  a simulation is easier and faster as less coupling has to be considered. A principal quantum number of  $n = 22$  is a good choice, as the frequency distance between the high- $l$  manifold and lower  $l$ -states is higher than in the case of larger principal quantum numbers. Thus, an easier analysis of the experimental data is possible in terms of fitting the Rydberg lines. This will be described later on. While the f-state quantum defect is known [23], the g-state quantum defect, up to this point is only known to be in a certain range [10, 11]. Based on the experimental data, it has been possible to extract a more accurate value of the g-state quantum defect.

### 4.2.1 Electric field dependent measurement

The procedure to set up a Stark map measurement is based on the general procedure described in subsection 3.5.2. The UV and the green transition are locked to the transition wavelengths of the branches chosen (see table 3.5.1 and 3.5.2). The green transition is chopped and the lock-in amplifier's parameters are the same as for the pressure dependent measurements, which are in turn based on previous investigations as described in subsection 3.4.2. Thus, the lock-in amplifier's time constant is 30 ms. Here, the scan velocity of the Rydberg laser is set in the interface to 30 GHz in 19.9 s. However, in the scope of further optimizations, no lock-in but the direct output of the TIA has been used to measure the Rydberg signal, allowing the increase in scan velocity by decreasing the scan time from 19.9 s to 1.9 s. This will be explained later on. A big scan range i.e. a periodic frequency detuning of the Rydberg laser of 30 GHz allows to measure the Stark

shift of the Rydberg lines in a large frequency range. The scan range is initially aligned such that the Rydberg state chosen and the splitting is clearly visible.

A pressure around  $70\ \mu\text{bar}$  has proven to be a good choice based on the pressure dependent investigations in the last chapter. On the one hand, the contribution of the collisional broadening to the linewidth is small, on the other hand good Rydberg signal in terms of SNR is gained. The pressure inside the cell is almost constant during the whole measurement run which is provided by the gas mixing setup including the MFCs. The Stark map measurements are done with pure NO, thus only the 5 sccm MFC is used. The flow is typically set between 1 sccm and 2 sccm, here the best flow stability is provided.

Like in the case of the pressure dependent measurements, the measurement run is done automatically using a Python script after the initial conditions are met. The Stark maps are typically measured starting from an offset voltage between the electrodes of  $-10\ \text{V}$  and increased in equally spaced steps to  $+10\ \text{V}$ , thus varying the electric field inside the cell between roughly  $-11.9\ \text{V/cm}$  and  $+11.9\ \text{V/cm}$ . The reason for the measurement with both negative and positive electric fields will be shown later. One might expect a mirror inversion at an offset voltage of  $0\ \text{V}$  of the Stark map which is in fact not the case in the experiment.

The step size if a lock-in is in use is typically  $+0.2\ \text{V}$ , leading to 101 single traces. This has proven to be a sensible compromise between a good resolution of the Stark map and the length of time of the measurement run, which is over two hours in this case.

After the Python script has set the offset voltage, the oscilloscope acquires the channels and the experimental parameters are saved as well. After that, the offset voltage is increased by one step and the procedure is repeated until the upper voltage limit is reached. Note, that in contrast to the pressure dependent measurements where a waiting time after setting a new flow value is necessary to achieve a stable pressure, the waiting time after setting the new offset voltage is negligible [52].

### 4.2.2 Evaluation

The evaluation routine of the Stark maps is based on the evaluation of the single traces as described in subsection 3.5.3. Afterwards, the single traces which differ by the electric field applied, are arranged on the  $x$ -axis. The  $x$ -axis shows the electric field and the  $y$ -axis shows the frequency providing the information by which the Rydberg laser has been detuned. The strength of the Rydberg signal is encoded in a non-linear color scheme to highlight the Rydberg lines. Depending on the direction of the electric field applied, the sign of the current changes. Negative electric fields correspond to a current with a positive sign. This is also considered in the Stark map. Further evaluation steps will be introduced in the scope of the results presented in subsection 4.2.3.

### 4.2.3 Results

Several different Stark maps starting from the rotational series  $N^+ = 6$  down to  $N^+ = 0$  for different principal quantum numbers including  $n = 22, 32, 42$  have been measured. This data is valuable for future theoretical investigations. Here, the lock-in amplifier has been used for the measurements.

In the following, a selection of highly resolved Stark maps is shown. Figure 4.2.1 shows the Stark map of the state 32(2). The high- $l$  manifold is clearly visible, as well as a straight line which is visible in the figure at a Rydberg laser detuning of roughly  $\Delta f = 12$  GHz. This line appears in every Stark map measured and cannot be explained based on theoretical simulations of the Stark effect in NO, but must be related to the electric field distribution inside. Apparently, there must be a residual electric field inside the cell. Since the behavior of the Rydberg lines does not change when crossing the aforementioned straight line, an interaction of the Rydberg lines with the straight line may be excluded. In the other case, so-called avoided crossings would appear. However, a more in-depth explanation cannot be given at this time.

Figure 4.2.2 shows a Stark map of the states 27(6) and 32(4). In figure 4.2.3 a Stark map of the states 42(2) and 35(4) is depicted. Due to the fact that the Rydberg states are nearby, both Rydberg states can be measured in one Stark map measurement run. Crossings of the Rydberg lines of the high- $l$  manifolds in high electric fields are visible.

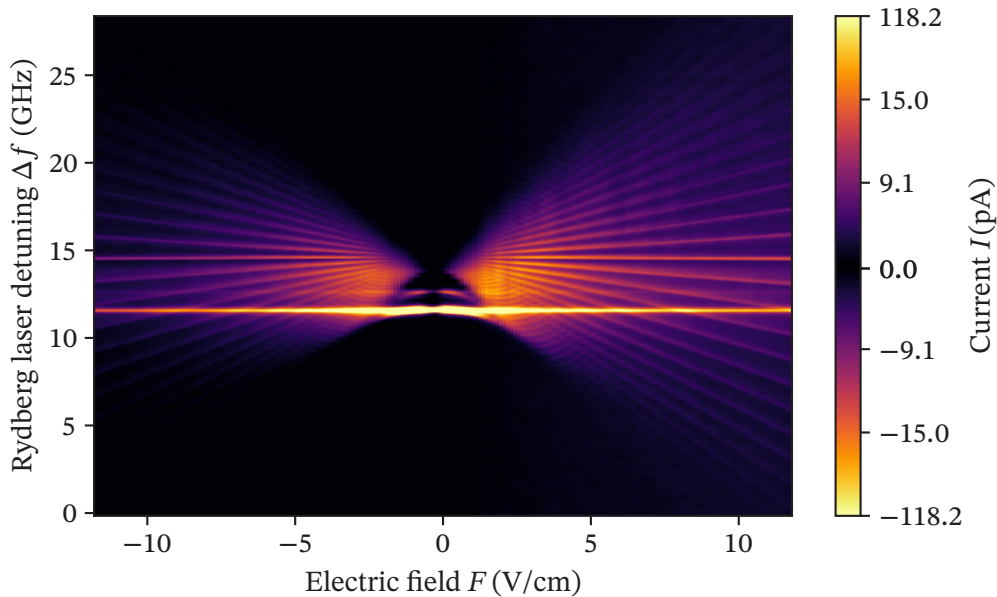


**Figure 4.2.1:** Stark map of the state 32(2).

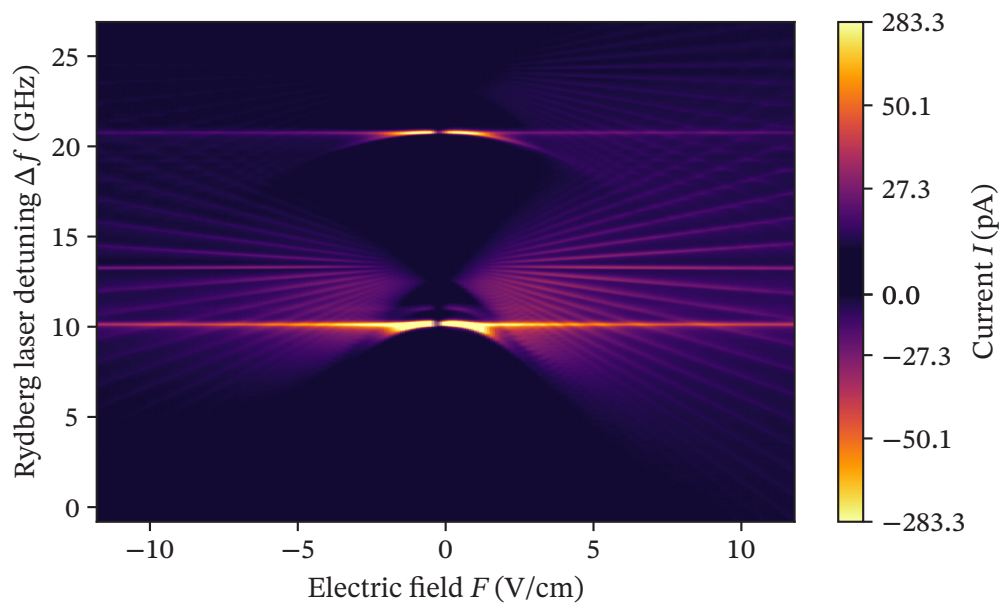


**Figure 4.2.2:** Stark map of the state 32(4) visible at a lower frequency detuning and the state 27(6) visible at a higher detuning.

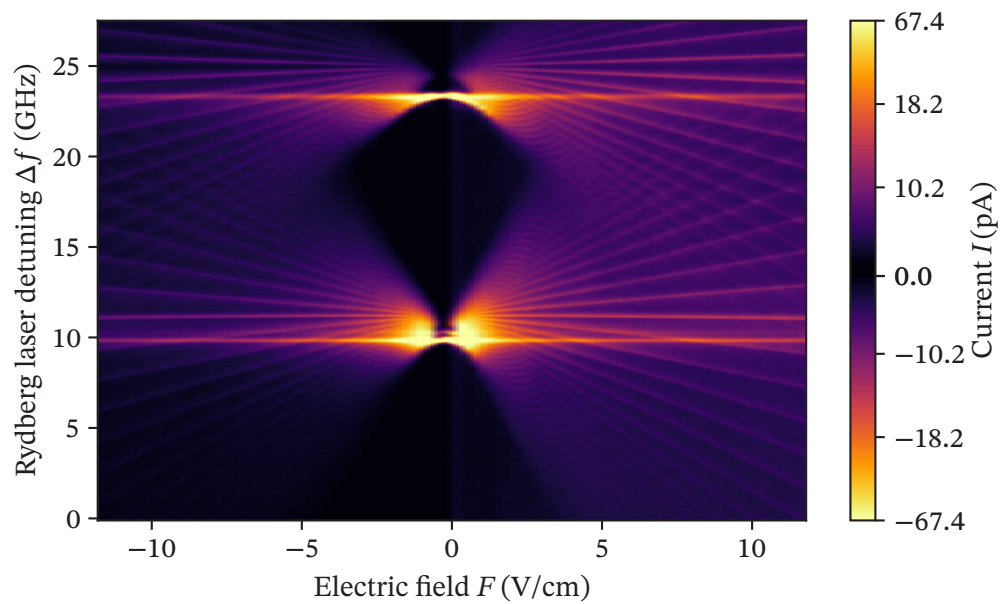


**Figure 4.2.3:** Stark map of the state 42(2) visible at a lower frequency detuning and the state 35(4) visible at a higher detuning.

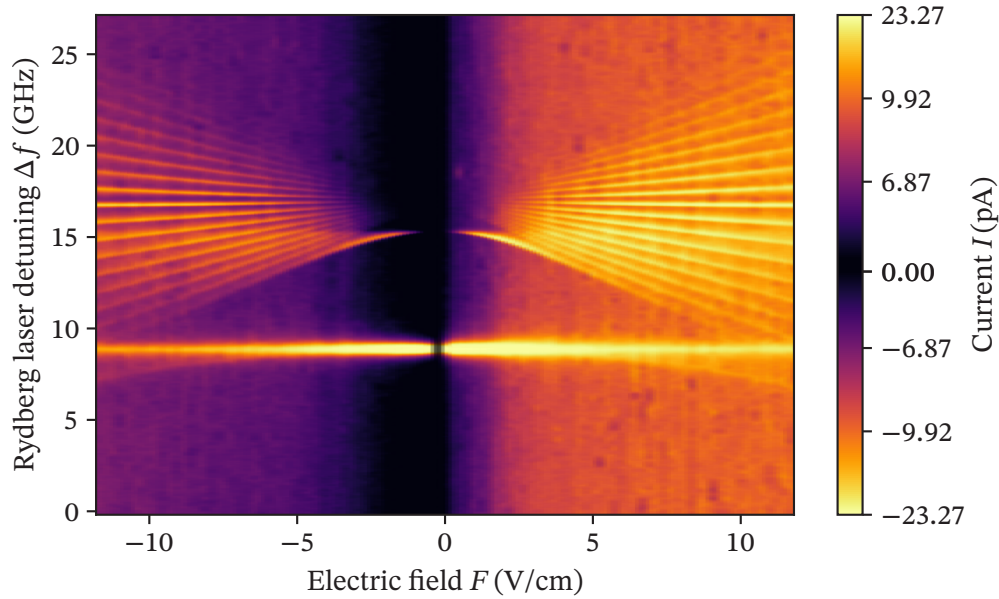


**Figure 4.2.4:** Stark Map of the 22(0). Due to low UV power, the currents measured are comparably low, which leads to a bad SNR despite the usage of a lock-in amplifier and chopping the green transition.

As already explained, the state of main interest is 22(0), since further analysis regarding theoretical simulations are easier to make. Like in the case of the other Stark maps shown, up to this point the lock-in amplifier has been used and the green transition chopped. The Stark map of the state 22(0) is visible in figure 4.2.4. However, due to the degradation of the pump laser of the UV laser system, the resolution in terms of SNR is bad due to small ionization currents, compared to the Stark maps presented before, despite the fact that a lock-in amplifier has been used.

For that reason, some optimizations have been made. First of all, the green, as well as the infrared laser beam have been focused into the cell using appropriate lenses. The UV laser beam was already focused into the cell for the measurements done before, due to the bad laser mode. The volume inside which the excitation to the Rydberg states is occurring is the one where all three laser beams overlap. Thus, the size of the volume is limited by the laser beam with the smallest waist. The UV laser beam has a  $1/e^2$  beam waist of about  $940 \mu\text{m}$ , the green laser beam has a waist of about  $640 \mu\text{m}$ , and the infrared one has a beam waist of  $1200 \mu\text{m}$  [20] before they were focused into the cell. The beam waists after focusing, inside the cell, have been roughly estimated to be  $25 \mu\text{m}$  for the UV,  $140 \mu\text{m}$  for the green, and  $90 \mu\text{m}$  for the infrared laser beam. These values can be seen as the lower bounds of the actual beam waists. Focusing the green and the infrared laser beams led to a significant increase in the excitation efficiency despite the very low UV power. Therefore, no lock-in amplifier is required anymore to gain a sufficiently high quality of the Stark map. Now, for the Stark map measurement, the Rydberg signal

recorded is the direct output of the TIA on the cell and not the lock-in amplifier's output as it is not used anymore.

A crucial factor of the Stark map measurements has been the duration of the measurements. Because the measurement data of the state  $22(0)$  should provide the data for new determinations, the resolution of the Stark map is further improved by taking more single traces, i.e. the step size of the voltage between the electrodes during the measurement run is reduced. The step size of choice is now  $+0.05$  V instead of  $+0.2$  V as before. This might extend the duration of the measurement run, however, the Rydberg laser scan time is reduced too because no limitations due to the lock-in amplifier have to be faced. The Rydberg laser scan time of choice for the new Stark map measurement is  $1.9$  s which is roughly ten times faster than before. This value can be justified by a rough estimation. The possible scan time of the Rydberg laser has a lower limit due to the rise and fall time of the TIA. Assuming a lower bound of the Rydberg linewidth of around  $70$  MHz, the laser's integration time of the Rydberg signal is

$$t_{\text{Ryd}} = \frac{1.9 \text{ s} \cdot 70 \text{ MHz}}{30 \text{ GHz}} = 4.43 \text{ ms}, \quad (4.11)$$

which is around 36 times the TIA's time constant  $\tau = 121 \mu\text{s}$ . To reach 99% of the Rydberg signal's maximum, an integration time of roughly  $5\tau$  is enough. Due to technical reasons, a lower scan time is not used. The main contribution to the duration of the measurement run is now the time it takes to save the data acquired by the oscilloscope.

Comparing to the scan velocity of  $30$  GHz in  $19.9$  s as chosen for the Stark map measurements before, involving a lock-in amplifier, leads to an integration time of the laser of  $t_{\text{Ryd, lock-in}} = 46.43$  ms. This comparably large integration time of the laser has been necessary due to the lock-in amplifier's parameters chosen, i.e. a time constant of  $30$  ms and low pass filter slope of  $18 \text{ dB oct}^{-1}$ . Further details are described in [52].

The final Stark map of the state  $22(0)$  taken after the optimization process is visible in figure 4.2.7. Here, the TIA's output is recorded directly and no lock-in amplifier is in use. Compared to the Stark map of  $22(0)$  showed in figure 4.2.4, the peak ionization current is over twenty times larger now, leading to a significant improvement of the quality of the Stark map.

Starting from this point, a more in-depth treatment of the Stark map is made. The highest currents detected in the Stark map of  $22(0)$  are the ones in the f-state at an absolute value of the electric field roughly between  $0.5$  V/cm and  $2$  V/cm. Exemplary, two single traces of the Stark map at different electric fields are shown. In the case of a low electric field, the Stark splitting is not yet visible, see figure 4.2.6. The f- and g-state are distinguishable. In the case of high electric fields, several Rydberg lines due to the Stark effect appear, which can be seen in the single trace in figure 4.2.7.

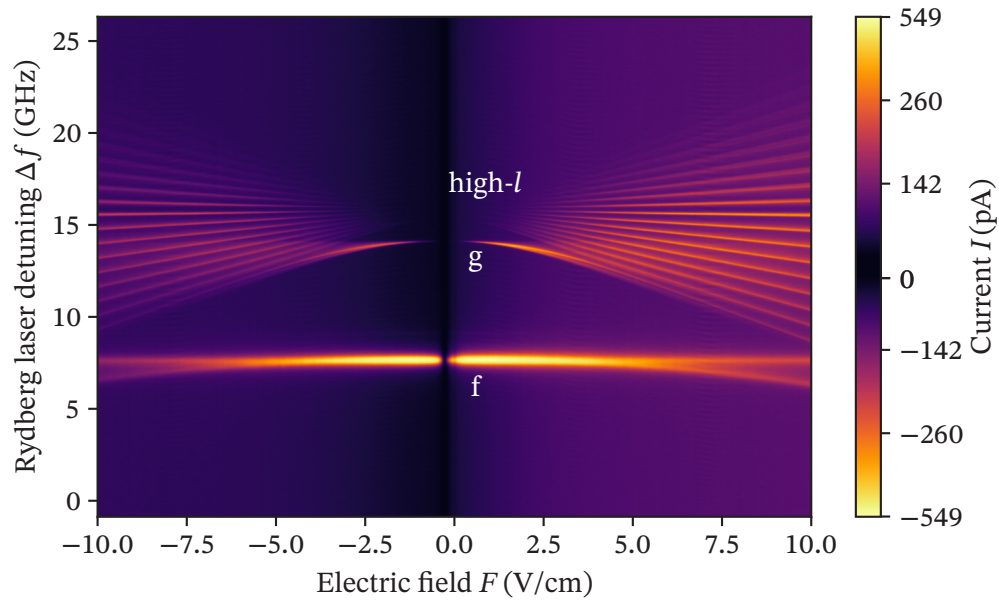


**Figure 4.2.5:** A high-resolution Stark map of 22(0) after optimization. Here, no lock-in amplifier is involved.

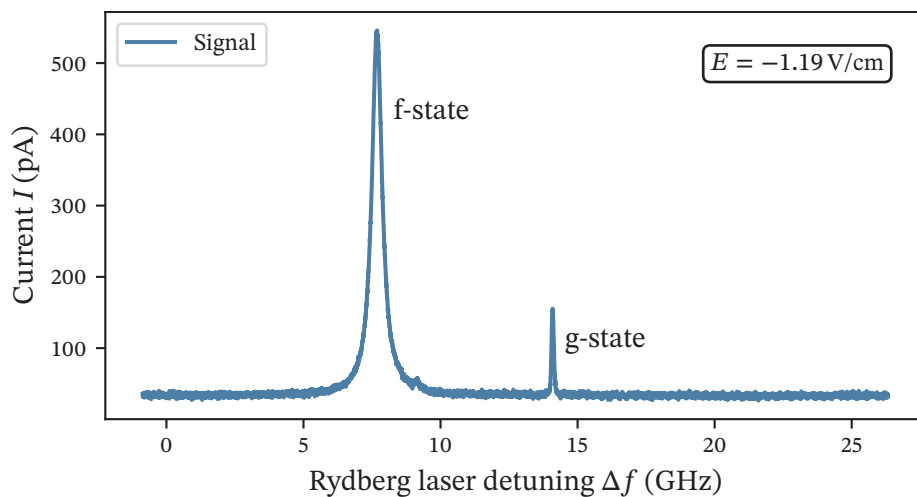


**Figure 4.2.6:** Single trace from the Stark map visible in 4.2.5 at a low electric field. Here, the Stark splitting is just about to occur. The f- and g-state are labeled.

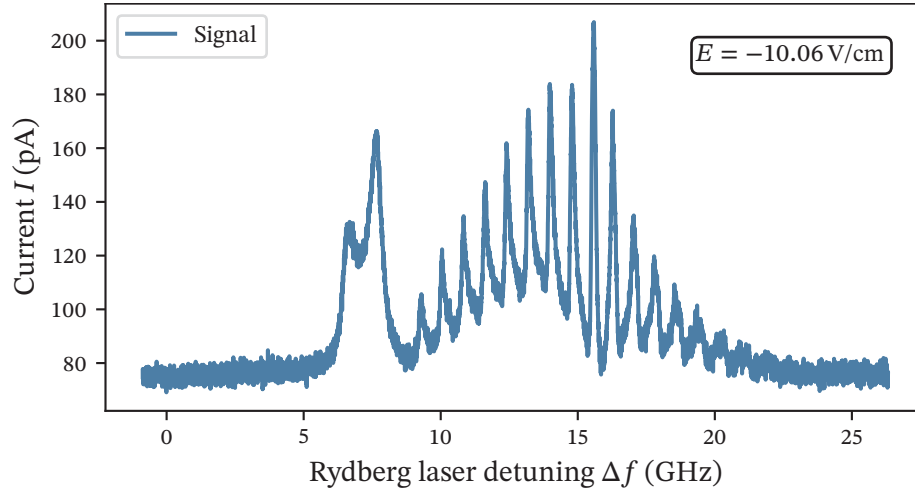


**Figure 4.2.7:** Single trace from the Stark map visible in 4.2.5 at a high electric field. Compared to the single trace at low electric fields (figure 4.2.6) the splitting of the states is clearly visible resulting in several Rydberg lines.

At this point it is important to note, why the Stark maps have been measured with both positive and negative electric fields. If one has a look at the Stark map in figure 4.2.5, the actual zero-field position i.e. the symmetry axis is slightly shifted to negative electric fields. This might be attributed to the different times of flight (TOF) of the charges to the electrodes after the ionization. In [51] an estimation supposing an offset voltage of  $-10$  V has been made. In this case, the TOF is up to  $1.59 \mu\text{s}$  for the nitrosyl cation  $\text{NO}^+$  and  $6.8$  ns for the electron. Surface and space charges contribute to the non-linearity of the electric field inside the cell [51]. The symmetric Stark map measurements allow a better analysis of the experimental data as will be shown next.

In the following, a short guideline is given on how the quantum defects are extracted based on the experimental data. The idea is to align the simulated data in such a way, that it represents the experimental data properly. A crucial parameter is the electric field inside the cell.

In the first step, the Rydberg lines of several single traces of the Stark map of the state  $22(0)$  are fitted using Lorentzian functions and the peak positions are extracted. Here, an iterative method is used. In order to perform the subsequent fitting routine, strong boundary conditions have to be set to keep track of the right line to fit in the Stark map. The fit function of choice is

$$\Delta f_{\text{fit}}(F) = A \cdot \sqrt{(F - F_{\text{offset}})^2 + F_{\text{stray}}^2} + \Delta f_{\text{off}}. \quad (4.12)$$

The result of the fitting routine is visible in the figure 4.2.8.  $A$  is a scaling factor. The offset of the symmetry axis of the Stark map measured is  $F_{\text{offset}}$ . The electric field

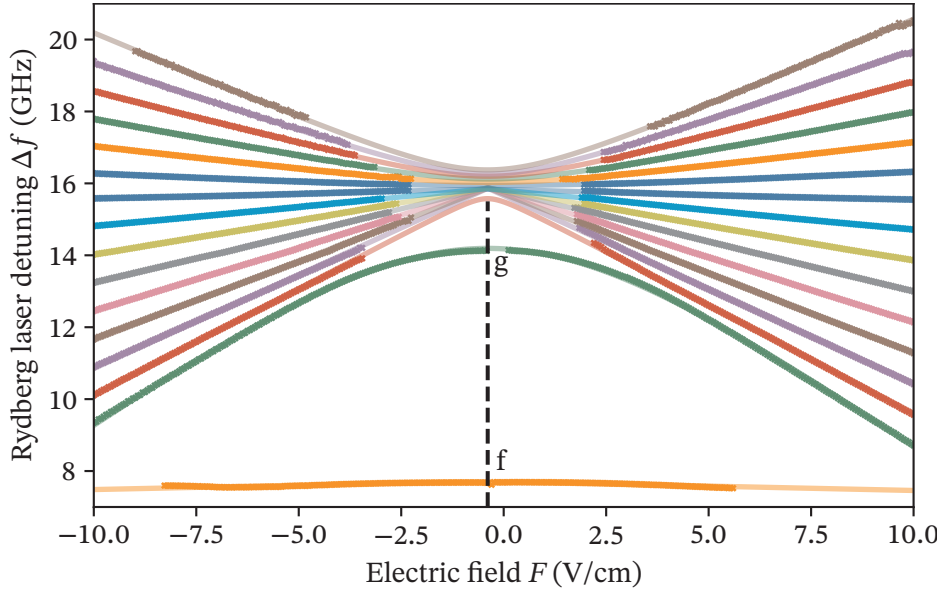


**Figure 4.2.8:** Zoom-in to the Stark map of the state 22(0) in figure 4.2.5. Here, the peak positions of the Rydberg lines, which were extracted from the experimental data, are fitted using equation (4.12). The electric field offset is indicated by the dashed black. The f-, g- and high- $l$  states are properly represented by the fits, which is supported by the fact that the extracted fit parameters have allowed to align the simulation to the experimental data, see figure 4.2.9.

between the electrodes is supposed to be zero here, however, there are residual stray fields perpendicular to the electric field axis which are considered by introducing  $F_{\text{stray}}$ .  $\Delta f_{\text{off}}$  describes the frequency offset on the  $y$ -axis. These are the fit parameters. The electric field offset is at about  $F_{\text{off}} \approx -0.390$  V/cm, and the stray fields are in a range of up to  $F_{\text{stray}} \approx 2.431$  V/cm.

The fit parameters extracted from the aforementioned fitting routine are used to align the simulation to the experimental data. Furthermore, the electric fields of the data simulated are scaled with factor 1.1 based on the investigations in [51]. For the simulation, the quantum number  $M_N = 3$  fits the best to the experimental data.  $M_N = 3$  is the highest reasonable value because mainly f-states are excited, see subsection 2.3.3 and section 2.5. The final simulation on top of the measured data after the alignment is shown in figure 4.2.9. The g-state quantum defect has been extracted by slowly adapting its value in the simulation. It has been adjusted to  $\delta_{g\Lambda}^{(b)} \approx 0.00296657$ . This value is not finalized yet and the uncertainty has not been estimated as well. The precision is expected to be comparably high to the precision of the quantum defects known, see table 2.3.1.

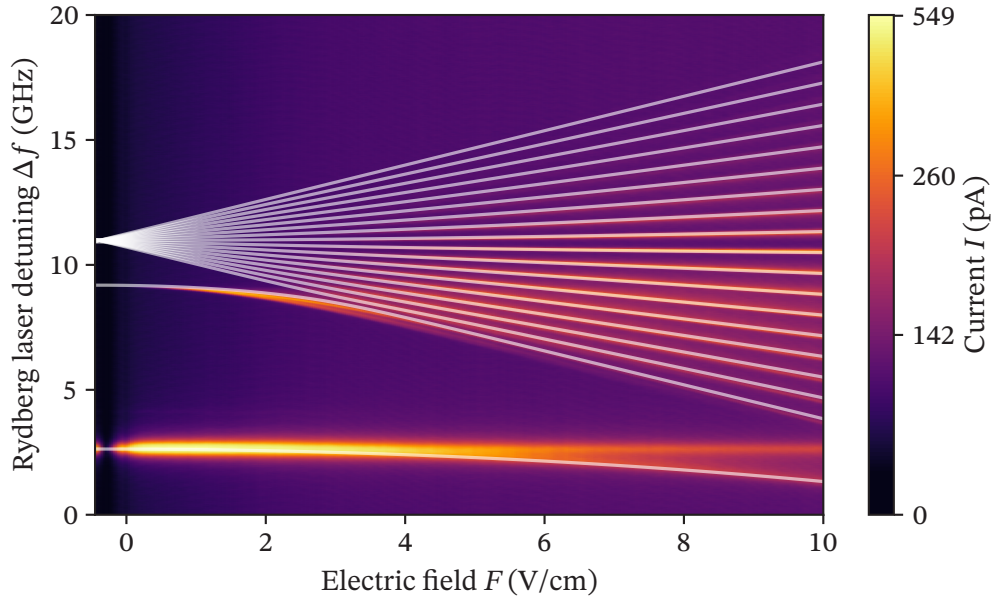


**Figure 4.2.9:** Zoom-in to the Stark map of the state 22(0) in figure 4.2.5. The simulated and aligned data is plotted in white color on the top and is in very good agreement with the experimental data which allows to deduce the g-state quantum defect.

#### 4.2.4 Conclusion

Regarding the sensor application, electric fields between 0.5 V/cm and 2 V/cm and the f-state might be a good choice as these fields and this  $l$ -state lead to the highest Rydberg signals, if referring to the Stark map measurement of the state 22(0). Optimizations have been made to improve the quality of the Stark maps. Based on the cooperation providing the theory to the Stark map measurements, it has been possible to assign a more precise value to the quantum defect of the g-state. The data available in the literature [10, 11] states that the g-state quantum defect is in the range between 0.002 and 0.004. Based on the new experimental data and the simulations a more accurate value has been attributed to the g-state quantum defect, namely  $\delta_{g\Lambda}^{(b)} \approx 0.00296657$ . However, this result is not finalized yet. The experimental data of several Stark maps of different Rydberg states will serve as a database for further theoretical investigations in the future.

## 5 Summary and outlook

In the scope of this work, an optogalvanic trace-gas sensor has been optimized for subsequent investigations of Rydberg states in nitric oxide (NO).

In the first part, collisional broadening and shifts of Rydberg lines in NO have been studied. Regarding a sensor application, an operation in the mikrobar regime is desirable to minimize broadening effects due to collisions. Elastic collisions are more dominating in the case of NO perturbed by itself, compared to the perturbation of NO with nitrogen ( $N_2$ ). In the first case, a red shift has been observed, if the density of NO is increased. In the case of perturbation of NO with an increasing density of  $N_2$  only a slight blue shift has been visible in the density range investigated. Fermi has shown, that the linear density dependency of the shift might be attributed to elastic collisions between the Rydberg electron and the perturber [7]. The shift rates extracted from our measurements with pure NO are in the same order of magnitude, but a multiple smaller when compared to investigations involving alkalis perturbed by rare gas atoms [8, 9]. On the other hand, our broadening rates are higher. The differences might be explained based on the complexity of the rovibrational molecular spectrum. In contrast to a molecule, atoms do not have vibrational and rotational degrees of freedom.

In the second part, the Stark effect of several Rydberg states has been investigated. Optimizations concerning the experimental parameters have been done, finally leading to a highly resolved Stark map of the Rydberg state with the principal quantum number  $n = 22$  and the rotational series  $N^+ = 0$ . Taking the non-linear electric field in the experimental measurement cell into account, it has been possible to align a theoretical simulation of the Stark map to the experimental data. The simulation has been done by Prof. Stephen Hogan and Dr. Matthew Rayment at the University College London (UCL). Finally, the g-state quantum defect has been extracted and is now given to a higher precision as in the literature ([10, 11]). Nevertheless, the result for the g-state quantum defect is not finalized yet.

In the future, improvements to the trace-gas sensor's properties will be made. Here, optimizations concerning the design and the electrical circuit of the measurement cell may lead to a higher sensitivity. To improve the sensitivity other rotational branches for the excitation have to be considered, as other excitation paths may lead to higher Rydberg signals. Further improvements to the sensor's sensitivity could allow the detection of the NO bimolecule as shown in [4]. However, future investigations will be based upon the results of this work, as they provide the information concerning good experimental parameters.



# Danksagung

An dieser Stelle möchte ich einigen Personen danken, die wesentlich zum erfolgreichen Abschluss meiner Masterarbeit beigetragen haben.

**Prof. Dr. Tilman Pfau** für die Möglichkeit im QNOSE-Team am PI5 meine Masterarbeit zu schreiben.

**Fabian Munkes** für die umfangreiche Unterstützung und Betreuung meiner Arbeit.

**Dr. Harald Kübler** für die Unterstützung und Koordinierung des Projekt.

**Florian Anschütz** für die Unterstützung bei den Messungen.

**Philipp Neufeld**, dass er mich auf das Projekt aufmerksam gemacht hat und die Betreuung am Anfang.

Außerdem bedanke ich mich bei den bereits erwähnten Mitgliedern des Teams, sowie **Ettore Eder**, **Yannick Schellander** und **Maurice Schamber** für eine angenehme Arbeitsatmosphäre während meiner Masterarbeit.



## Bibliography

- [1] S. M. Andrabi et al. “Nitric oxide: physiological functions, delivery, and Biomedical Applications”. In: *Advanced Science* 10.30 (2023), p. 2303259 (cit. on pp. i, 1).
- [2] L. E. Gustafsson et al. “Endogenous nitric oxide is present in the exhaled air of rabbits, guinea pigs and humans”. In: *Biochemical and biophysical research communications* 181.2 (1991), pp. 852–857 (cit. on pp. i, 1).
- [3] K. Alving, E. Weitzberg, and J. Lundberg. “Increased amount of nitric oxide in exhaled air of asthmatics”. In: *European Respiratory Journal* 6.9 (1993), pp. 1368–1370 (cit. on pp. i, 1).
- [4] R. González-Férez, J. Shertzer, and H. Sadeghpour. “Ultralong-Range Rydberg Bimolecules”. In: *Physical Review Letters* 126.4 (2021), p. 043401 (cit. on pp. i, iii, 1, 63).
- [5] D. Barredo et al. “Electrical readout for coherent phenomena involving Rydberg atoms in thermal vapor cells”. In: *Physical Review Letters* 110.12 (2013), p. 123002 (cit. on pp. i, 1).
- [6] J. Schmidt et al. “Proof of concept for an optogalvanic gas sensor for NO based on Rydberg excitations”. In: *Applied Physics Letters* 113.1 (2018) (cit. on pp. i, 1).
- [7] E. Fermi. “Sopra lo spostamento per Pressione delle Righe Elevate delle Serie Spettrali”. In: *Nuovo Cim* 11 (1934), pp. 157–166 (cit. on pp. ii, 2, 20–22, 43, 63).
- [8] C. Füchtbauer, P. Schulz, and A. Brandt. “Verschiebung von hohen Serienlinien des Natriums und Kaliums durch Fremdgase, Berechnung der Wirkungsquerschnitte von Edelgasen gegen sehr langsame Elektronen”. In: *Zeitschrift für Physik* 90.5-6 (1934), pp. 403–415 (cit. on pp. ii, 43, 51, 63).
- [9] K. Weber and K. Niemax. “Impact broadening and shift of Rb nS and nD levels by noble gases”. In: *Zeitschrift für Physik A Atoms and Nuclei* 307.1 (1982), pp. 13–24 (cit. on pp. ii, 43, 51, 63).
- [10] A. Goodgame et al. “The Stark effect in the  $v+=1$  autoionizing Rydberg states of NO”. In: *The Journal of chemical physics* 116.12 (2002), pp. 4922–4937 (cit. on pp. ii, 12, 53, 62, 63).
- [11] A. Fujii and N. Morita. “Three-color triple resonance spectroscopy of highly excited Rydberg states of NO: Decay dynamics of high- $l$  Rydberg states”. In: *The Journal of chemical physics* 103.14 (1995), pp. 6029–6039 (cit. on pp. ii, 53, 62, 63).
- [12] T. A. Popov. “Human exhaled breath analysis”. In: *Annals of Allergy, Asthma & Immunology* 106.6 (2011), pp. 451–456 (cit. on p. 2).

- [13] H. Haken and H. C. Wolf. *Molekülphysik und Quantenchemie - Einführung in die experimentellen und theoretischen Grundlagen*. Wiesbaden: Springer Berlin Heidelberg, 2006. ISBN: 978-3-540-30314-5 (cit. on pp. 3, 4, 7, 11).
- [14] J. M. Brown and A. Carrington. *Rotational Spectroscopy of Diatomic Molecules*. Cambridge: Cambridge University Press, 2003. ISBN: 978-0-521-53078-1 (cit. on pp. 3, 7–9, 14).
- [15] M. Born and W. Heisenberg. “Zur Quantentheorie der Molekeln”. In: *Annalen der Physik* 379.9 (1924), pp. 1–31 (cit. on p. 3).
- [16] P. M. Morse. “Diatomic molecules according to the wave mechanics. II. Vibrational levels”. In: *Physical review* 34.1 (1929), p. 57 (cit. on p. 6).
- [17] G. Herzberg. *Molecular Spectra and Molecular Structure - Vol I*. Bd. 1. Read Books Limited, 2013. ISBN: 9781446549148. URL: <https://books.google.de/books?id=W2Z8CgAAQBAJ> (cit. on pp. 7–9, 11, 13–15, 20, 21).
- [18] L. B. Maia and J. J. Moura. “Detection of nitric oxide by electron paramagnetic resonance spectroscopy: spin-trapping with iron-dithiocarbamates”. In: *Plant Nitric Oxide: Methods and Protocols* (2016), pp. 81–102 (cit. on p. 10).
- [19] J. Brown, A. Cole, and F. Honey. “Magnetic dipole transitions in the far infra-red spectrum of nitric oxide”. In: *Molecular Physics* 23.2 (1972), pp. 287–295 (cit. on p. 11).
- [20] F. Munkes. “Electrical detection of Rydberg interactions in nitric oxide at room temperature”. PhD thesis. 5th Institute of Physics, University of Stuttgart, 2023 (cit. on pp. 11, 13–15, 22, 30–33, 36, 39, 42, 43, 48, 57).
- [21] N. Šibalic and C. S. Adams. “Rydberg physics”. In: *Rydberg physics* (2018), pp. 2399–2891 (cit. on p. 12).
- [22] W. Demtröder. *Experimentalphysik 3: Atome, Moleküle und Festkörper*. Springer-Lehrbuch. Springer Berlin Heidelberg, 2016. ISBN: 9783662490945. URL: <https://books.google.de/books?id=tR5kDAAAQBAJ> (cit. on p. 12).
- [23] M. Rayment and S. Hogan. “Quantum-state-dependent decay rates of electrostatically trapped Rydberg NO molecules”. In: *Physical Chemistry Chemical Physics* 23.34 (2021), pp. 18806–18822 (cit. on pp. 12–14, 25, 39, 53).
- [24] R. Patel, N. Jones, and H. Fielding. “Observation of the Stark effect in  $v+=0$  Rydberg states of NO with a matrix-diagonalization analysis”. In: *Journal of Physics B: Atomic, Molecular and Optical Physics* 40.7 (2007), p. 1369 (cit. on p. 13).
- [25] D. Albritton, A. Schmeltekopf, and R. Zare. “Potential energy curves for NO+”. In: *The Journal of Chemical Physics* 71.8 (1979), pp. 3271–3279 (cit. on p. 13).
- [26] J. Brown et al. “The labeling of parity doublet levels in linear molecules”. In: *Journal of Molecular Spectroscopy* 55.1-3 (1975), pp. 500–503 (cit. on p. 14).

- [27] P. Kaspar et al. “Doppler-free high-resolution continuous-wave optical UV spectroscopy on the  $A^2\Sigma^+ \leftarrow X^2\Pi_{3/2}$  transition in nitric oxide”. In: *Physical Review A* (2022). ISSN: 2469-9926, 2469-9934. DOI: 10.1103/PhysRevA.106.062816. URL: <https://link.aps.org/doi/10.1103/PhysRevA.106.062816> (visited on 07/18/2023) (cit. on p. 14).
- [28] Western. *PGOPHER version 10.1*. University of Bristol Research Data Repository, 2018 (cit. on pp. 14, 39).
- [29] S. Dixit et al. “Rotational branching ratios in (1+ 1) resonant-enhanced multi-photon ionization of NO via the  $A \Sigma^+ 2$  state”. In: *Physical Review A* 32.2 (1985), p. 1267 (cit. on p. 14).
- [30] K. Kaufmann, C. Nager, and M. Jungen. “Rydberg states and quantum defects of the NO molecule”. In: *Chemical physics* 95.3 (1985), pp. 385–390 (cit. on p. 14).
- [31] Y. Ogi et al. “Laser-induced amplified spontaneous emission from the 3d and nf Rydberg states of NO”. en. In: *Chemical Physics* 255.2-3 (May 2000), pp. 379–395. ISSN: 03010104. DOI: 10.1016/S0301-0104(00)00043-4. URL: <https://linkinghub.elsevier.com/retrieve/pii/S0301010400000434> (visited on 07/24/2023) (cit. on pp. 14, 15, 39).
- [32] D. X. Wang, C. Haridass, and S. P. Reddy. “The Gamma ( $A2\Sigma^+-X2\Pi_r$ ) System of the Nitric Oxide Isotopomers”. In: *Journal of Molecular Spectroscopy* 175.1 (1996), pp. 73–84 (cit. on p. 15).
- [33] S. Mollet, F. Merkt, and F. Merkt. *Rydberg States and Photoionisation Dynamics of NO and Cl2*. ETH, 2013. URL: <https://books.google.de/books?id=rpFJngEACAAJ> (cit. on p. 15).
- [34] W. Demtröder. *Laserspektroskopie 1: Grundlagen*. SpringerLink : Bücher. Springer Berlin Heidelberg, 2011. ISBN: 9783642213069. URL: <https://books.google.de/books?id=huOfBAAAQBAJ> (cit. on p. 17).
- [35] A. Fox. *Quantum Optics: An Introduction*. Oxford Master Series in Physics. OUP Oxford, 2006. ISBN: 9780198566724. URL: <https://books.google.de/books?id=2YESDAAAQBAJ> (cit. on p. 17).
- [36] C. Foot and O. Press. *Atomphysik*. De Gruyter, 2020. ISBN: 9783110669121. URL: <https://books.google.de/books?id=3pY9EAAAQBAJ> (cit. on p. 17).
- [37] J. J. Olivero and R. Longbothum. “Empirical fits to the Voigt line width: A brief review”. In: *Journal of Quantitative Spectroscopy and Radiative Transfer* 17.2 (1977), pp. 233–236 (cit. on p. 17).
- [38] T. Gallagher. *Rydberg Atoms*. Cambridge Monographs on Atomic, Molecular and Chemical Physics. Cambridge University Press, 1994. ISBN: 9780521385312. URL: <https://books.google.de/books?id=8JIpEhHWT-cC> (cit. on pp. 19, 20).
- [39] E. Amaldi and E. Segrè. “Effect of pressure on high terms of alkaline spectra”. In: *Nature* 133.3352 (1934), pp. 141–141 (cit. on p. 20).

- [40] M. L. Cohen. “The Fermi atomic pseudopotential”. In: *American Journal of Physics* 52.8 (1984), pp. 695–703 (cit. on pp. 20, 21).
- [41] C. R. Gould and E. I. Sharapov. “Fermi’s favorite figure: the history of the pseudopotential concept in atomic physics and neutron physics”. In: *The European Physical Journal H* 47.1 (2022), p. 10 (cit. on p. 20).
- [42] H. S. Friedrich. *Theoretical Atomic Physics* -. Wiesbaden: Springer Berlin Heidelberg, 2017. ISBN: 978-3-540-81004-9 (cit. on p. 23).
- [43] L. Kador, D. Haarer, and R. Personov. “Stark effect of polar and unpolar dye molecules in amorphous hosts, studied via persistent spectral hole burning”. In: *The Journal of chemical physics* 86.10 (1987), pp. 5300–5307 (cit. on pp. 23, 24).
- [44] F. Munkes. *Continuous-wave absorption spectroscopy on the  $X^2\Pi_{3/2}$  to  $A^2\Sigma^+$  transition of nitric oxide*. Master’s thesis. 5th Institute of Physics, University of Stuttgart, 2019 (cit. on p. 28).
- [45] J. Lekavich. “Basics of acousto-optic devices”. In: *Lasers & Applications* (1986), pp. 59–64 (cit. on p. 31).
- [46] I. Chang. “Acousto-optic devices and applications”. In: *Handbook of optics 2* (1995), pp. 12–1 (cit. on p. 31).
- [47] E. D. Black. “An introduction to Pound–Drever–Hall laser frequency stabilization”. In: *American journal of physics* 69.1 (2001), pp. 79–87 (cit. on pp. 32, 33).
- [48] P. Pruy. *Aufbau eines frequenzstabilisierten Masterlasers für Transfercavities*. Bachelor’s thesis. 5th Institute of Physics, University of Stuttgart, 2019 (cit. on p. 33).
- [49] M. Seltenreich. *Eigenschaften eines digitalen, vielseitigen und erweiterbaren Systems zur Laserfrequenzstabilisierung*. Bachelor’s thesis. 5th Institute of Physics, University of Stuttgart, 2021 (cit. on pp. 33, 40).
- [50] P. Kaspar. “Continuous wave Doppler-free spectroscopy on the  $A^2\Sigma^+ \leftarrow X^2\Pi_{3/2}$  transition in thermal nitric oxide”. PhD thesis. 5th Institute of Physics, University of Stuttgart, 2022 (cit. on pp. 34, 35).
- [51] E. Eder. *Entwicklung und Optimierung des elektrischen Feldes in einer Durchflusszelle zur Detektion von Rydbergzuständen in Stickstoffmonoxid*. Bachelor’s thesis. 5th Institute of Physics, University of Stuttgart, 2023 (cit. on pp. 36, 60, 61).
- [52] F. Anschütz. *Optimierung eines Messsignals eines Spurengassensors für Stickstoffmonoxid mittels einer zweistufigen Lock-In Technik*. Bachelor’s thesis. 5th Institute of Physics, University of Stuttgart, 2023 (cit. on pp. 37, 54, 58).
- [53] U. Tietze and C. Schenk. *Halbleiter-Schaltungstechnik*. Springer-Verlag, 2013 (cit. on p. 37).
- [54] J. Danielak et al. “Reinvestigation of the Emission  $\gamma$  Band System ( $A^2\Sigma^+ - X^2\Pi$ ) of the NO Molecule”. In: *Journal of Molecular Spectroscopy* 181.2 (1997), pp. 394–402 (cit. on p. 39).

- [55] F. Munkes et al. “Collisional shift and broadening of Rydberg states in nitric oxide at room temperature”. In: *arXiv preprint arXiv:2310.18256* (2023) (cit. on pp. 43, 52).
- [56] J. Shaffer and H. Kübler. “A read-out enhancement for microwave electric field sensing with Rydberg atoms”. In: *Quantum Technologies 2018*. Vol. 10674. SPIE. 2018, pp. 39–49 (cit. on p. 47).
- [57] M. N. Hughes. “Relationships between nitric oxide, nitroxyl ion, nitrosonium cation and peroxyxynitrite”. In: *Biochimica et Biophysica Acta (BBA)-Bioenergetics* 1411.2-3 (1999), pp. 263–272 (cit. on p. 50).
- [58] W. R. Hindmarsh, A. Petford, and G. Smith. “Interpretation of collision broadening and shift in atomic spectra”. In: *Proceedings of the Royal Society of London. Series A. Mathematical and Physical Sciences* 297.1449 (1967), pp. 296–304 (cit. on p. 52).



# Ehrenwörtliche Erklärung

Hiermit versichere ich gemäß §24.7 der Prüfungsordnung 2015,

1. dass ich die vorliegende Arbeit selbstständig verfasst habe,
2. dass ich keine anderen als die angegebenen Quellen benutze und alle wörtlich oder sinngemäß aus anderen Werken übernommenen Aussagen als solche gekennzeichnet habe,
3. dass die eingereichte Arbeit weder vollständig noch in wesentlichen Teilen Gegenstand eines anderen Prüfungsverfahrens gewesen ist, und
4. dass das elektronische Exemplar mit den anderen Exemplaren übereinstimmt.

Weiterhin erkläre ich gemäß der Handreichung für Studierende in den Lehreinheiten Mathematik und Physik der Fakultät 8 zur Verwendung von IT-/KI-gestützten Schreib- und Programmierwerkzeugen bei studentischen Arbeiten vom November 2023, dass ich beim Einsatz von IT-/KI-gestützten Schreibwerkzeugen diese Werkzeuge als verwendete Hilfsmittel mit ihrem Produktnamen, meiner Bezugsquelle und einer Übersicht des im Rahmen dieser Arbeit genutzten Funktionsumfangs vollständig aufgeführt habe. Bei der Erstellung dieser Arbeit habe ich durchgehend eigenständig und beim Einsatz IT-/KI-gestützter Schreibwerkzeuge steuernd gearbeitet. Eine Aufzählung findet im Folgenden statt.

1. Die deutsche Zusammenfassung wurde unter Zuhilfenahme des Online-Tools DeepL Translate, erreichbar unter <https://www.deepl.com/translator> erstellt.
2. Eine Rechtschreibprüfung der gesamten Arbeit wurde mittels der Visual Studio Code Extension namens Grammarly gemacht, auch online erreichbar unter <https://www.grammarly.com/>.

Stuttgart, den 22. Dezember 2023

Alexander Trachtmann